lene glycol-*bis*(2-aminoethyl)-*N,N,N,N*-tetraacetic acid (EGTA) (Ca^{2+}-free BSS).

Construction of Lentivirus Vectors Expressing Interfering Short Hairpin RNA (shRNAi) and Microglial Transduction

Lentivirus containing shRNAi was prepared by the method previously described (Yogosawa et al., 2005). The self-inactivating (SIN) vector construct pCS-RfA-CG, which contains the EGFP gene under the control of the CMV promoter and sites for site-specific recombination with a Gateway vector (attR1,2), was used for simultaneous expression of EGFP and shRNA. Plasmid containing $P2X_4R$ shRNAi under the control of human U6 promoter was provided by Dr. K. Inoue (Kyushu Univ. Fukuoka, Japan). The gene of the $P2X_4R$ shRNAi-expressing cassette inserted into pENTR™1A was transferred into the pCS-RfA-CG by a recombination reaction using Gateway LR Clonase (Invitrogen). The sequence of shRNA targeted for firefly luciferase was used as a control (Nishitsuji et al., 2004). The sequence was inserted into the piGENE™ hU6 *Bsp*MI vector (iGENE Therapeutics, Tsukuba, Japan), and the gene of the luciferase shRNAi-expressing cassette was ligated into the pCS-RfA-CG. The sequence of $shP2X_4R$ was: 5′-GGG ATA AGA GAT ATA GGT AAC GTG TGC TGT CCG TTA CTT ATA TTT CTT GTC CCT TTT T-3′. We confirmed the specificity of P2×4R shRNAi by a coexpression assay. pCS-shP2×4R-CG was cotransfected into Cos7 cells with P2×4 expression plasmid (provided by Dr. K. Inoue) or HA-tagged P2Y12R plasmid (Supplemental information). pCS-shP2×4R-CG significantly suppressed P2×4R expression but had no effect P2Y12R expression. The recombined plasmid was cotransfected into 293FT cells (Invitrogen) with a packaging plasmid (pCAG-HIVgp) and a plasmid expressing Rev and vesicular stomatitis virus G glycoprotein (pCMV-VSV-G-RSV-Rev), and the supernatant was collected after 48 h and filtered through a 0.45-μm pore filter (Falcon). Viral particles in the supernatant were concentrated by ultracentrifugation for 2 h at 19,400 rpm (SW28 rotor; Beckmann Coulter, CA) and recovered by suspension in Hanks buffered saline (Invitrogen).

The recombinant lentivirus (2×10^5 infectious units) was added to the mixed glial cells that had been cultured for 12 days in a 25-cm^2 flask, and cultured for 6 days in DMEM containing 10% FCS. Floating cells were collected as microglia and allowed to attach to appropriate dishes or glasses. The efficiency of microglia transduction with the $shP2X_4R$ vector was 20–30%, the same as with the shControl vector according to an analysis of the number of microglia expressing EGFP by flow cytometry.

Isolation of EGFP-Positive Microglia

After transduction with the lentivirus vectors, floating cells collected as microglia were resuspended in PBS containing 2% FCS. EGFP-positive and -negative cells were sorted with a FACSVantageSE flow cytometry system (BD Biosciences). Live gating was performed with propidium iodide (Sigma-Aldrich, St. Louis, MO). The purity of the EGFP-positive cells was >99% according to a flow cytometry analysis.

Western Blot Analysis of P2X Receptor Expression

Sorted cells were lysed in SDS sample buffer. $P2X_4R$, $P2X_7R$, EGFP, and actin proteins in the lysate equivalent to 2×10^4 cells were separated by 10% SDS-PAGE and detected by Western blot analysis with 1 μg/mL anti-$P2X_4R$ antibody (Alomone Labs, Jerusalem, Israel), 0.6 μg/mL anti-$P2X_7R$ (Alomone Labs), anti-GFP antibody (diluted 1:1,000, Medical & Biological Laboratories, Nagoya, Japan), and anti-actin antibody (diluted 1:1,000, Sigma), respectively, and visualized with the ECL system.

RT-PCR Analysis for $P2Y_{12}R$ Gene Transcripts

RNA was isolated from the sorted cells with the RNeasy Mini Kit (QIAGEN, Hildem, Germany) containing a DNase treatment, according to the manufacturer's protocols. Reverse transcription of RNA was performed with SuperScript III reverse transcriptase (Invitrogen). The PCR amplification conditions were 30 s at 94°C, 15 s at 60°C, and 30 s at 68°C for 25–35 cycles, except for the initial denaturation step of 2 min at 94°C and the final cycle with an elongation step of 5 min at 68°C. An extra reaction mixture without reverse transcriptase was used as a control for DNA contamination of the RNA sample. The primers used were as follows: rat $P2Y_{12}R$, 5′-AAA CTT CCA GCC CCA GCA ATC T-3′ (forward), 5′-CAA GGC AGG CGT TCA AGG AC-3′ (reverse); rat β-actin, as an internal standard, 5′-TTG TTA CCA ACT GGG ACG ACA TGG-3′ (forward), 5′-GAT CTT GAT CTT CAT GGT GCT AGG-3′ (reverse). PCR products of 447 bp for $P2Y_{12}R$ and 763 bp for β-actin were analyzed on a 1.5% agarose and stained with ethidium bromide. The relative intensity of the bands for $P2Y_{12}R$ was quantified by densitometry with NIH image software and normalized to the β-actin products. The normalized values were used to calculate the ratio of $P2Y_{12}R$ mRNA level in the EGFP-positive cells transduced with the $shP2X_4R$ vector to the level in the EGFP-positive cells transduced with the shControl vector.

Calcium Imaging

The intracellular calcium concentration ($[Ca^{2+}]_i$) was monitored by the fura-2 method described by Inoue et al. (1998), using a highly sensitive intensifier target video camera C2400 and an Argus 50 image processor (Hama-

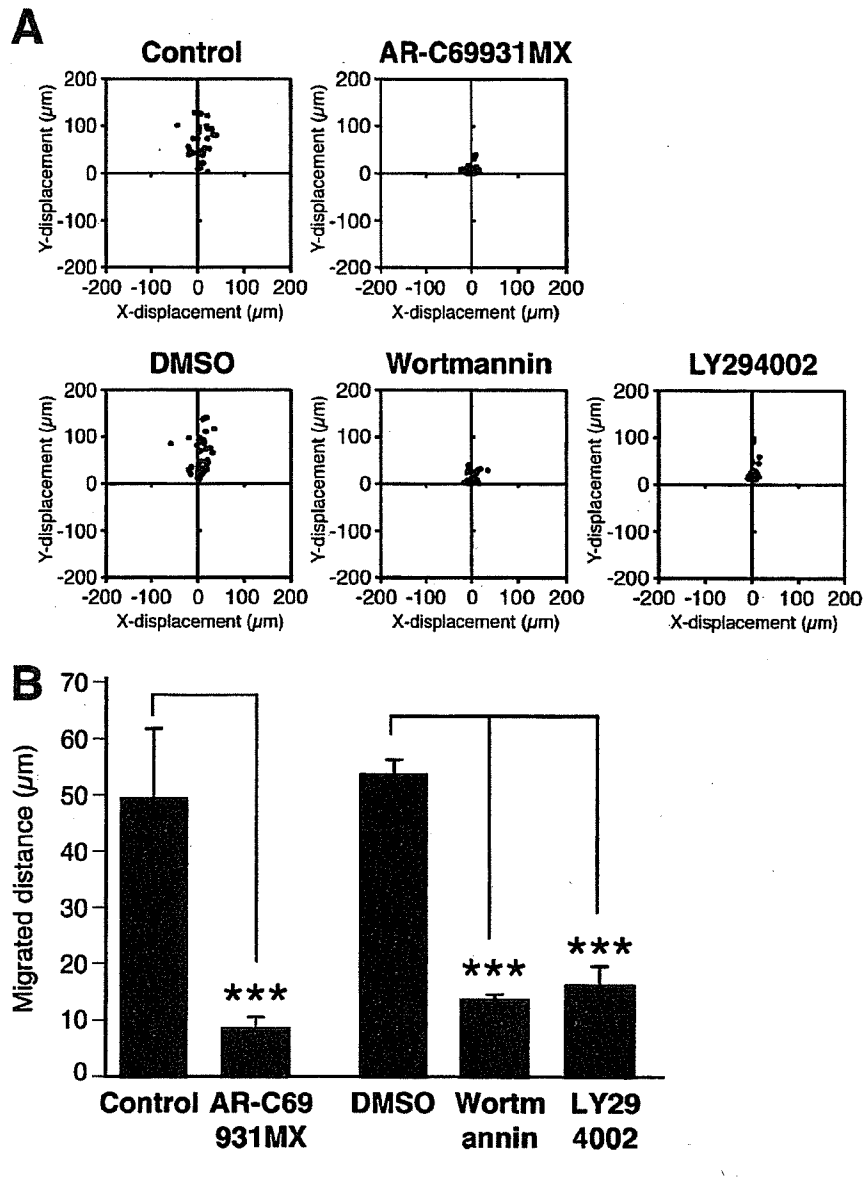

Fig. 1. Effect of PI3K inhibitors on ATP-induced microglial chemotaxis. (**A**) Microglia were pretreated with 1 μM AR-C69931MX for 10 min or with 0.125% DMSO, 100 nM wortmannin, or 50 μM LY294002 for 20 min, and microglial migration towards 50 μM ATP was observed in the Dunn chemotaxis chamber. The distance and direction migrated by individual cells are shown as x and y coordinates on scatter diagrams. The position of the outer well of the chamber is at the top in the vector diagrams of cells. (**B**) Chemotaxis by each cell was quantified by measuring the (x, y) distance migrated from the starting position. Data are means ± SD of three independent experiments. $^{***}P < 0.001$, Student's t-test.

matsu Photonics). Microglia transduced with the lentivirus vectors were plated at 2×10^5 cells/well on poly-L-lysine-coated CELLocate microgrid coverslips (Eppendorf, Hambrug, Germany). After 2 h, the cells were incubated with 10 μM fura-2 acetoxymethylester (fura-2/AM, Dojindo Laboratories, Kumamoto, Japan) at 37°C for 30 min in DMEM containing 25 mM HEPES (DMEM-H, Invitrogen), and the coverslips were mounted on an inverted epifluorescence microscope (TMD-300, Nikon, Tokyo, Japan). The cells were exposed to drugs dissolved in DMEM-H by superfusion. Raw data were recorded as 500-nm emissions of fura-2 excited alternately at 340 and 380 nm, and $[Ca^{2+}]_i$ was expressed as the ratio of the fluorescence intensity at 340 nm to the fluorescence intensity at 380 nm (F340/380).

RESULTS

Involvement of the PI3K Pathway in ATP-Induced Microglial Chemotaxis

We previously reported that ATP-induced microglial membrane ruffling were inhibited by treatment with pertussis toxin and a $P2Y_{12}R$-selective antagonist, AR-C69931MX, suggesting that Gi/o-coupled $P2Y_{12}R$ is involved in both the membrane ruffling and the chemotaxis (Honda et al., 2001). Stimulation of $P2Y_{12}R$ has been reported to induce PI3K activation (Czajkowski et al., 2004; Soulet et al., 2004; Van Kolen and Slegers, 2004). To determine whether PI3K activation is required for chemotaxis by ATP-stimulated microglia, we investigated the effects of the PI3K inhibitors wortmannin and

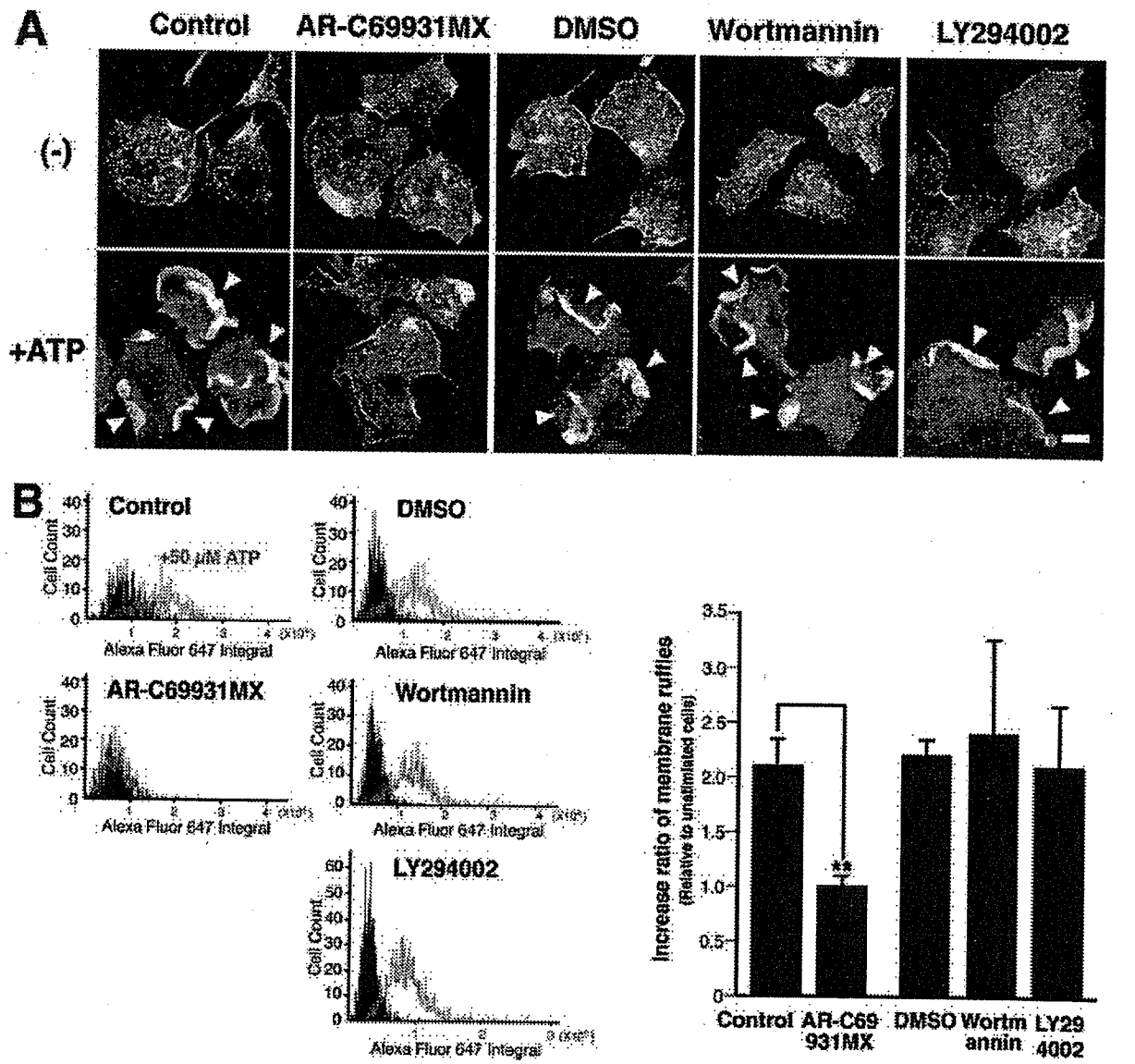

Fig. 2. Effect of PI3K inhibitors on ATP-induced microglial membrane ruffling. (A) Microglia were pretreated with 1 μM AR-C69931MX, 0.125% DMSO, 100 nM wortmannin, or 50 μM LY294002 as described in Fig. 1A, and then stimulated with 50 μM ATP for 5 min. After fixation, the cells were stained with Texas Red-conjugated phalloidin to visualize membrane ruffles. Arrowheads indicate membrane ruffles. Scale bar, 10 μm. (B) Quantification of membrane ruffles. Microglia were stimulated as in A for 5 min, fixed, and stained with an anti-Iba1 antibody and Alexa Fluor 647-conjugated phalloidin to recognize individual microglial cells and membrane ruffles, respectively. The F-actin content of microglial cells was quantified as integral intensity of Alexa Fluor 647 fluorescence by using LSC. The five panels on the left side are histograms representing the total F-actin in each cell (*x*-axis, Alexa fluor 647 integral) and the number of scanned cells (*y*-axis, cell count). The black region represents the unstimulated cells, and the region surrounded by the red line represents the ATP-stimulated cells. The bar graph on the right side shows the ratio of the mean of fluorescent intensity of ATP-stimulated cells to that of unstimulated cells after treatment with each inhibitor. Data are means ± SD of three independent experiments. $^{**}P < 0.01$, Student's *t*-test.

LY294002 with a Dunn chemotaxis chamber. Microglial chemotaxis toward the higher concentration of ATP was evaluated by analysis of time-lapse images. When 50 μM ATP was applied to the outer well, the cells migrated toward higher concentrations of ATP. Pretreatment of the microglia with wortmannin or LY294002 significantly blocked the chemotaxis (Fig. 1A). The chemotactic movement of the microglia was quantified by calculating the (*x*, *y*) distances individual cells migrated toward ATP. As shown in Fig. 1B, the mean distance migrated by cells pretreated with PI3K inhibitors was significantly shorter than the distance migrated by cells pretreated with DMSO. Treatment with 1 μM AR-C69931MX also inhibited the chemotaxis, as expected based on the results of our previous study (Honda et al., 2001). These findings suggested that PI3K activation is necessary for ATP-induced microglial chemotaxis.

Next, we investigated the effect of PI3K inhibitors on ATP-induced microglial membrane ruffling. As shown in Fig. 2A, phalloidin staining clearly demonstrated that ATP stimulation caused membrane ruffling within 5 min. Pretreatment of microglia with AR-C69931MX inhibited the ATP-induced membrane ruffling, as reported previously (Honda et al., 2001). However, exposure to 100 nM wortmannin or 50 μM LY294002 appeared to have no effect on the membrane ruffling. To confirm the effect of PI3K inhibitors on membrane ruffling quantitatively, the increase in F-actin in cells with membrane ruffles was analyzed with a laser scanning cytometer (LSC), which is a microscope-based cytometer. ATP-stimulated and unstimulated cells were stained with an anti-Iba1 antibody and Alexa Fluor 647-conjugatde phalloidin, and F-actin content was quantified by calculating the mean Alexa Fluor 647 fluorescent intensity of individual cells positive for a microglial marker protein Iba1 (Ito et al., 1998). As shown in Fig. 2B, the mean fluorescent intensity of control microglia was increased approximately 2-fold by ATP stimulation. The fluorescent intensity of ATP-stimulated cells pretreated with AR-C69931MX did not change significantly; however, the fluorescent intensity of cells pretreated with wortmannin or LY294002 was increased by ATP stimulation the same as in the control and the DMSO-treated cells. These results indicate that PI3K activation is not required for the membrane ruffling, but is necessary for induction of microglial chemotaxis.

ATP-Induced Akt Phosphorylation and Effect of Extracellular Calcium Deprivation

To determine whether the PI3K pathway in microglia is activated by ATP stimulation, we investigated Akt phosphorylation, a downstream signaling for PI3K (Bellacosa et al., 1991; Scheid and Woodgett, 2003), by Western blot analysis with a phospho-specific Akt antibody. ATP stimulation rapidly increased the level of Akt phosphorylation in a time-dependent manner (Fig. 3A), and pretreatment with 1 μM AR-C69931MX or 100 nM wortmannin inhibited the increase in Akt phosphorylation (Figs. 3B,C). These results indicated that ATP induces activation of the PI3K/Akt cascade in microglia and that the activation is mediated by P2Y$_{12}$R.

Previous studies (Inoue et al., 1998; Tsuda et al., 2003) have shown that stimulation of microglia with 50 μM ATP induces a transient increase in $[Ca^{2+}]_i$ that depends on the presence of extracellular Ca^{2+}, suggesting that ionotropic P2X receptors are responsible for the Ca^{2+} response. Use of the Ca^{2+}-sensitive fluorescent dye fura-2 revealed that the chelation of extracellular Ca^{2+} suppressed the ATP (50 μM)-evoked increase in $[Ca^{2+}]_i$ in our cultured microglia (data not shown). To determine whether the increase in $[Ca^{2+}]_i$ had any effect on the PI3K/Akt activation, we investigated Akt phosphorylation in microglia stimulated with 50 μM ATP in the absence of extracellular Ca^{2+}, and as shown in Fig. 4, chelation of extracellular Ca^{2+} by EGTA significantly

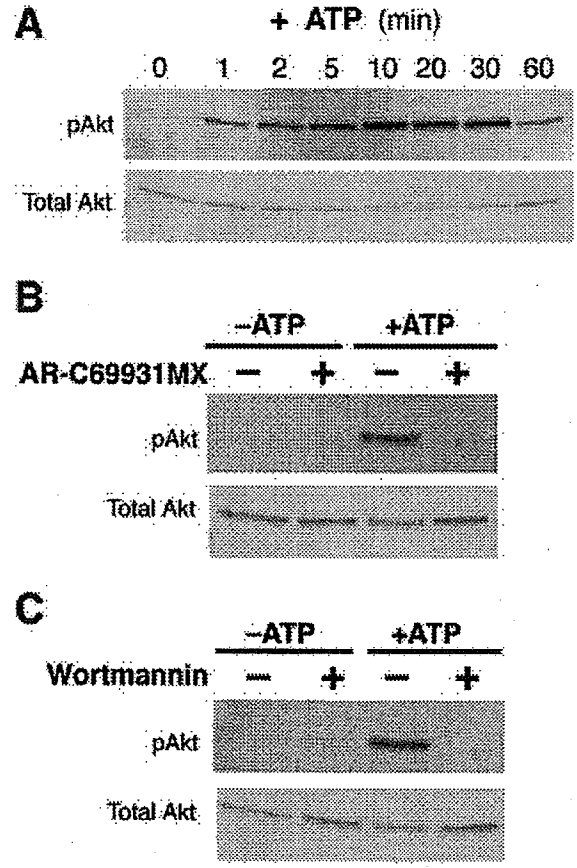

Fig. 3. ATP-induced Akt phosphorylation in microglia is dependent on PI3K activation through P2Y$_{12}$R. (A) Microglia were stimulated with 50 μM ATP for the period of time indicated and then lysed in SDS sample buffer. Phosphorylated (pAkt) and total Akt in the lysates were detected by Western blot analysis. (B, C) Microglia were pretreated with 1 μM AR-C69931MX for 10 min (B) or with 100 nM wortmannin for 20 min (C) and then stimulated with 50 μM ATP for 5 min. Akt phosphorylation was detected by Western blot analysis. Similar results were obtained from three independent experiments.

decreased ATP-induced Akt phosphorylation. Previous studies have shown that M-CSF stimulates the Fms tyrosine kinase receptor to activate Akt in macrophages in a PI3K-dependent manner (Comalada et al., 2004; Weiss-Haljiti et al., 2004). M-CSF also stimulated Akt phosphorylation in microglia, but chelation of extracellular Ca^{2+} had no effect on it (Fig. 4). These results led us to speculate that the ATP-induced PI3K/Akt activation, which is an essential component for induction of microglial chemotaxis, was linked to an increase in $[Ca^{2+}]_i$ through the extracellular Ca^{2+}-influx via ionotropic P2X receptors.

Effect of P2XR Antagonists on ATP-Induced Microglial Chemotaxis and Akt Phosphorylation

Since primary-cultured microglia have been shown to express P2X$_4$R (Tsuda et al., 2003; Xiang and Burnstock,

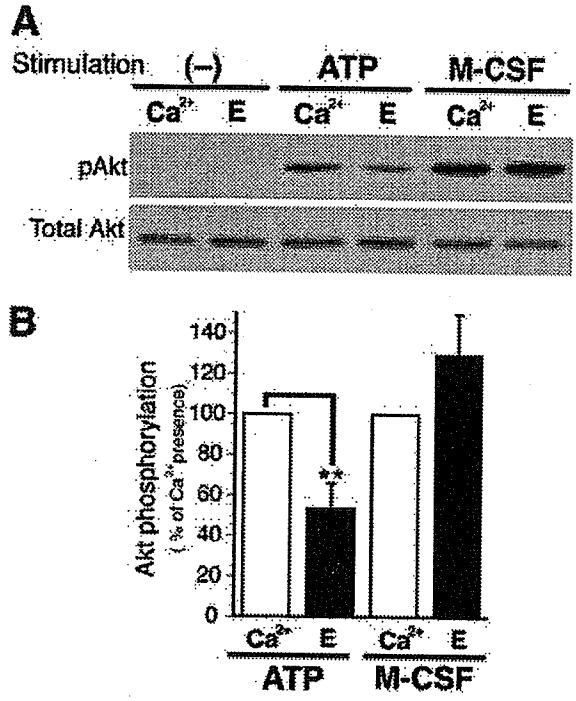

Fig. 4. Inhibitory effect of chelation of extracellular calcium on ATP-stimulated Akt phosphorylation. (A) Microglia were incubated for 30 min in BSS containing 1.2 mM Ca^{2+} (Ca^{2+}) or 1 mM EGTA (E) and then stimulated with 50 μM ATP or 100 ng/mL M-CSF for 5 min. Akt phosphorylation was detected by Western blot analysis. (B) The Akt phosphorylation level was quantified by densitometry. The results are expressed as percentage of agonist-induced phosphorylation in the presence of Ca^{2+} and are means ± SD of three independent experiments. $^{**}P < 0.01$; Student's *t*-test.

2005) and $P2X_7R$ (Ferrari et al., 1996; Nörenberg et al., 1994; Verkhratsky and Kettenmann, 1996; Walz et al., 1993), we first investigated the involvement of P2XRs in microglial chemotaxis with a $P2X_{1-4}R$, antagonist TNP-ATP, with a $P2X_{1,2,3,5,7}R$ antagonist PPADS, and with a selective $P2X_7R$ antagonist BBG. After pretreatment with an antagonist for 5 min the microglia were observed for chemotactic movement toward ATP in a Dunn chemotaxis chamber containing the antagonist. Treatment with 100 μM TNP-ATP appeared to suppress the ATP-induced microglial chemotaxis, but 300 μM PPADS or 1 μM BBG had no effect (Fig. 5A). The chemotactic movement of the microglia was quantified by calculating the mean value of the total (x, y) distances of individual cells migrated toward ATP. As shown in Fig. 5B, the mean distance migrated by the cells pretreated with TNP-ATP was significantly shorter than the distance migrated by the control cells, but the values of the cells pretreated with PPADS or BBG were not significantly different from those of the controls. Treatment with 1 μM AR-C69931MX also completely inhibited the chemotaxis. These results suggested that $P2X_4R$ as well as $P2Y_{12}R$ is involved in ATP-induced microglial chemotaxis.

We next examined the effect of the three P2XR antagonists, TNP-ATP, PPADS, and BBG, on ATP-stimulated Akt phosphorylation. TNP-ATP significantly suppressed the ATP-stimulated Akt phosphorylation, but PPADS or BBG appeared to have no effect (Fig. 6). AR-C69931MX also completely inhibited Akt phosphorylation. These results suggested that ATP-induced PI3K/Akt activation is mediated by $P2X_4R$ as well as $P2Y_{12}R$.

Downregulation of $P2X_4R$ in Microglia by Short Hairpin $P2X_4R$ RNAi

To determine whether $P2X_4R$ is in fact involved in ATP-induced microglial chemotaxis, we suppressed $P2X_4R$ expression in microglia with RNAi. We constructed a lentivirus vector that expresses both short hairpin (sh)-RNAi and EGFP under the control of the U6 RNA polymerase III promoter and the CMV promoter, respectively (Fig. 7A), and thus cells expressing the shRNAi should also express the EGFP reporter. Microglia were transduced with a lentivirus vector expressing a short hairpin $P2X_4R$ RNAi ($shP2X_4R$) or a control vector that expressed short hairpin luciferase RNAi (shControl). Lentiviral particles were added to mixed glial cell cultures, and floating cells were collected as microglia. To confirm the suppression of $P2X_4R$ expression by $shP2X_4R$, EGFP-positive cells were sorted with a flow cytometer, and expression of $P2X_4R$ protein in the cell lysate was investigated by Western blot analysis with an anti-$P2X_4R$ antibody. $P2X_4R$ protein expression was markedly suppressed in the EGFP-positive cells transduced with $shP2X_4R$ (Fig. 7B), whereas there was no difference in $P2X_4R$ protein level between the EGFP-positive and EGFP-negative cells after transduction with shControl. $P2X_7R$ protein expression was unaffected by transduction with $shP2X_4R$ (Fig. 7B). Microglial RNA was isolated from the sorted cells, and $P2Y_{12}R$ mRNA levels were analyzed by RT-PCR and normalized against actin mRNA levels. $P2Y_{12}R$ mRNA levels increased linearly with PCR reactions for 25–35 cycles. When PCR reactions were performed for 27 cycles, there was no difference in relative level of $P2Y_{12}R$ mRNA in EGFP-positive cells between transduction with $shP2X_4R$ and transduction with shControl (ratio of $P2Y_{12}R$ mRNA level in the $shP2X_4R$-transduced cells to the shControl-transduced cells = 1.1, Fig. 7C). We checked the $P2Y_{12}R$ mRNA level amplified by PCR for 25 and 30 cycles and confirmed that the relative level of $P2Y_{12}R$ mRNA in the $shP2X_4R$-transduced cells was the same as in the shControl-transduced cells. These results indicated that $P2X_4R$ expression was specifically suppressed in the EGFP-positive microglia after transduction with $shP2X_4R$.

The increase in $[Ca^{2+}]_i$ induced by ATP (50 μM) in microglia has been shown to be mediated by $P2X_4R$ (Tsuda et al., 2003). To determine whether $shP2X_4R$ interfered with $P2X_4R$ function in the EGFP-positive microglia, the level of $[Ca^{2+}]_i$ in individual cells was monitored by imaging analysis with fura-2 after transduction with the lentivirus vectors. A 30-s application of 50 μM ATP produced an increase in the 340/380 emission ratio of fura-2 in the EGFP-positive cells transduced with the con-

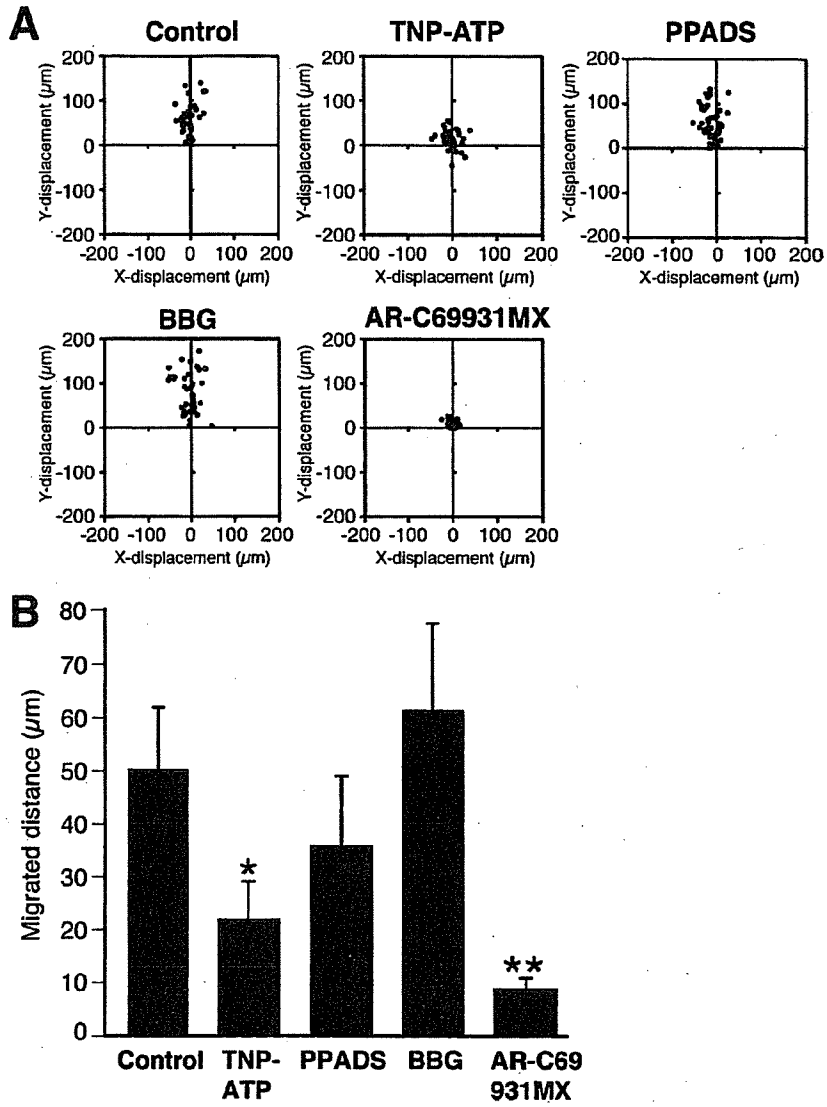

Fig. 5. Effect of P2X antagonists on ATP-induced microglial chemotaxis. (**A**) Microglia were pretreated with 100 μM TNP-ATP, 300 μM PPADS, or 1 μM BBG for 5 min or with 1 μM AR-C69931MX for 10 min. Microglial migration towards 50 μM ATP was observed in the Dunn chemotaxis chamber. The distance and direction of migration by individual cells are shown as x and y coordinates on scatter diagrams. (**B**) Chemotaxis was quantified by measuring the (x, y) distance migrated from the starting position of cells. Data are means ± SD of three independent experiments. $^{*}P < 0.05$, $^{**}P < 0.01$, Student's t-test.

trol vector (Fig. 8A left), whereas the increase in 340/380 emission ratio was significantly attenuated in the EGFP-positive cells transduced with shP2X$_4$R (Figs. 8A,B). These results confirmed that transduction with shP2X$_4$R downregulates expression of P2X$_4$R protein.

Effect of shP2X$_4$R on ATP-Induced Membrane Ruffling and Chemotaxis by Microglia

The effect of P2X$_4$R downregulation on ATP-induced membrane ruffling was examined in microglia transduced with the lentivirus vectors. EGFP-positive cells transduced with shP2X$_4$R or shControl developed membrane ruffles in response to ATP stimulation, the same as EGFP-negative cells (Fig. 9). These results indicated that shP2X$_4$R did not inhibit the activation of P2Y$_{12}$R and suggested that P2X$_4$R downregulation had no effect on ATP-induced membrane ruffling.

The cells transduced with the vectors were also examined for chemotactic movement in a Dunn chemotaxis chamber. As shown in the scatter diagrams, the migration of EGFP-positive cells transduced with shP2X$_4$R (Fig. 10A, bottom left) was clearly inhibited in comparison with the EGFP-negative cells (bottom right). EGFP-positive cells transduced with shControl (top left) migrated toward ATP as same as the EGFP-negative cells (top right). To quantify the effect of the shRNAi on the chemotactic movement of microglia, we calculated the mean value of the (x, y) distances EGFP-positive and -negative cells migrated toward ATP (Fig. 10B). The mean distance migrated by the EGFP-positive cells transduced with shP2X$_4$R was significantly shorter than both the mean distance migrated by the EGFP-negative cells and the mean distance migrated by the EGFP-positive cells

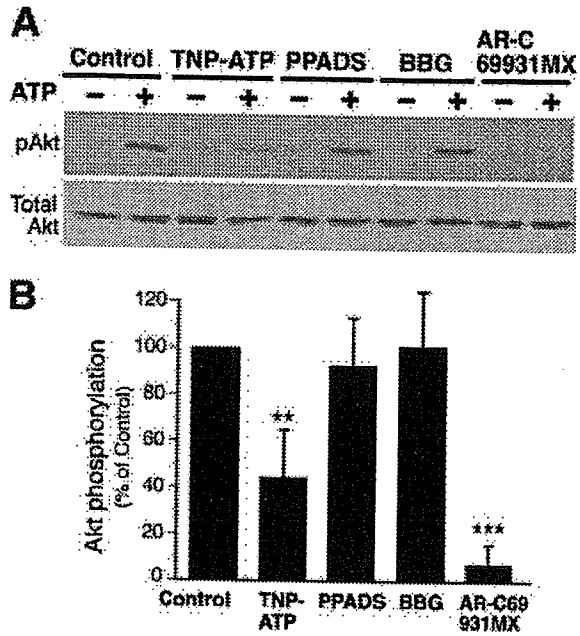

Fig. 6. Effect of P2X antagonists on ATP-stimulated Akt phosphorylation. (A) Microglia were pretreated with 100 μM TNP-ATP, 30 μM PPADS, or 100 nM BBG for 5 min or with 1 μM AR-C69931MX for 10 min, and then stimulated with 50 μM ATP for 5 min. Akt phosphorylation was detected by Western blot analysis. (B) The Akt phosphorylation level was quantified by densitometry and expressed as percentage of ATP-induced phosphorylation in control cells. The data shown are means ± SD of three independent experiments. $^{**}P < 0.01$, $^{***}P < 0.001$; Student's *t*-test.

transduced with shControl. There was no difference in distance migrated by the EGFP-positive cells and the EGFP-negative cells after transduction with shControl. These results clearly indicated that $P2X_4R$ is involved in ATP-induced microglial chemotaxis.

DISCUSSION

As expected from our previous findings (Honda et al., 2001), both the ATP-induced microglial membrane ruffling and chemotaxis were completely inhibited by a specific $P2Y_{12}R$ antagonist, AR-C69931MX, (Figs. 1 and 2). In this study we further investigated the signaling pathway downstream for $P2Y_{12}R$ and the effect of P2XR antagonists and shRNAi against $P2X_4R$ on microglial migration, and we found that $P2X_4R$ is also involved in ATP-induced microglial chemotaxis.

$P2Y_{12}R$ was known to be coupled to activation of PI3K and inhibition of adenylate cyclase (Czajkowski et al., 2004; Soulet et al., 2004; Van Kolen and Slegers, 2004), and Nasu-Tada et al. (2005) recently reported that a $P2Y_{12}R$-mediated decrease in cyclic AMP is an important step in membrane ruffling and chemotaxis by microglia on fibronectin-coated dishes. PI3K is well known to be a key player in remodeling of the actin cytoskeleton and in regulating cell migration, including chemotaxis (Procko and McColl, 2005; Van Haastert and Devreotes, 2004). In this study we showed that PI3K inhibitors

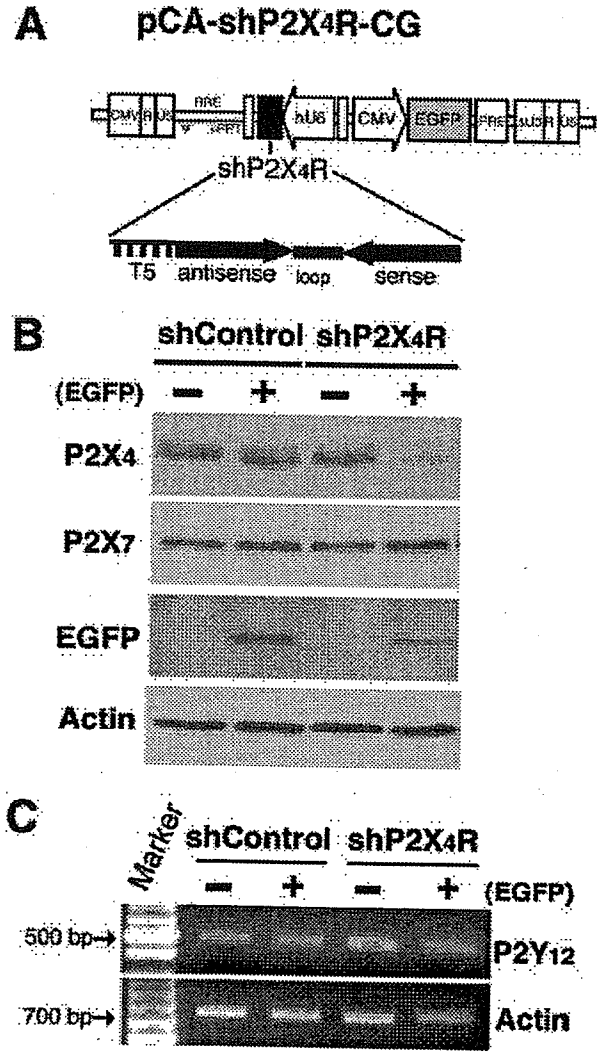

Fig. 7. shRNAi-targeted downregulation of $P2X_4R$ in microglia by lentivirus vectors. (A) Schematic drawing of lentivirus vectors expressing EGFP and shRNAi against $P2X_4R$ ($shP2X_4R$). A shRNA sequence targeted for firefly luciferase (shControl) was used as a control. (B) Protein expression of $P2X_4R$ and $P2X_7R$ in the microglia transduced with the shRNAi lentivirus vectors. EGFP-positive (+) and -negative (−) cells were sorted with a flow cytometer and lysed in SDS sample buffer. Protein expression of $P2X_4R$, $P2X_7R$, EGFP, and actin in the cell lysates was detected by Western blot analysis. Actin served as an internal control. (C) Gene transcript analysis of microglia transduced with the shControl or $shP2X_4R$ vector. RNA was isolated from the sorted cells. Gene transcripts for $P2Y_{12}R$ and β-actin, which served as an internal control, were analyzed by RT-PCR. The relative intensity of the bands for $P2Y_{12}R$ was quantified by densitometry and normalized to the β-actin products. Similar results were obtained from at least three independent experiments.

blocked microglial chemotaxis towards ATP (Fig. 1). However, the PI3K inhibitors had no effect on membrane ruffling (Fig. 2), suggesting that the initial actin reorganization induced by ATP is not dependent on PI3K activation, whereas the ATP gradient-dependent cell migration requires PI3K activation. PI3Ks phosphorylate phosphoinositides at the 3-hydroxyl of the inositol

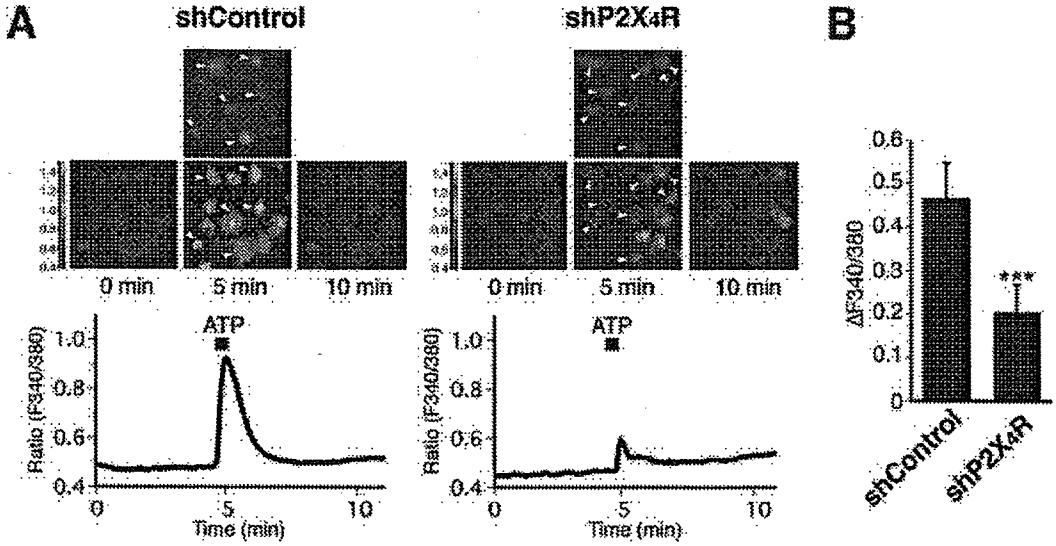

Fig. 8. Effect of P2X$_4$R downregulation on the ATP-evoked increase in $[Ca^{2+}]_i$ in microglia. (**A**) Microglia transduced with the shControl (left panel) or shP2X$_4$R (right panel) vector were loaded with fura-2/AM. $[Ca^{2+}]_i$ was expressed as the ratio of the fluorescence intensity at 340 nm to the fluorescence intensity at 380 nm (F340/380). The pseudocolor image shows three frames (0, 5, and 10 min) of fura2-loaded microglia stimulated with 50 μM ATP for 30 s. Arrowheads point to EGFP-positive cells. The traces show the mean increase in F340/380 emission ratio of 14 EGFP-positive cells from each culture. (**B**) The graphs show the relative increase in ratio (ΔF340/380; mean ± SD, n = 14 cells) from the basal level of the EGFP-positive cells shown in Fig. 8A. $^{***}P < 0.001$; Student's t-test. Similar results were obtained from three independent experiments.

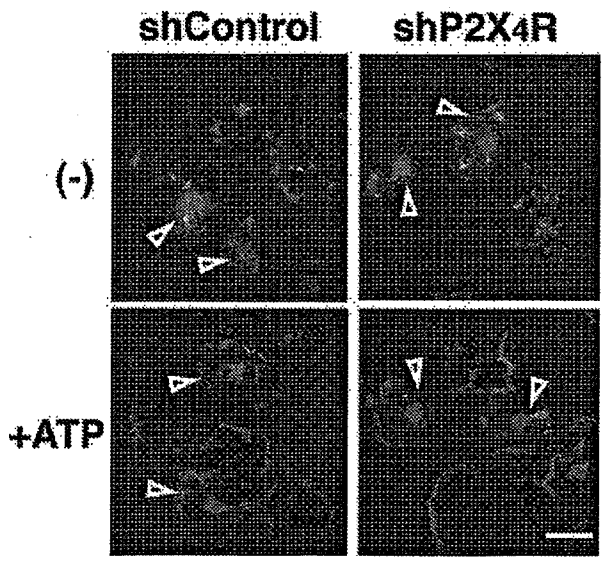

Fig. 9. Effect of P2X$_4$R downregulation on ATP-induced membrane ruffling of microglia. Microglia transduced with the lentivirus vectors were stimulated with 50 μM ATP for 5 min. After fixation, the cells were stained with Texas Red-conjugated phalloidin. Arrowheads indicate EGFP-positive cells. ATP-stimulated membrane ruffling of EGFP-positive cells were observed in three independent experiments. Scale bar, 20 μm.

ring (Vanhaesebroeck et al., 2001). When cells are placed in a chemoattractant gradient, the phosphorylated phospholipids selectively accumulate at the leading edge and act as a membrane anchor for many PI3K downstream effector proteins with pleckstrin homology (PH) regions, which may regulate directional sensing during chemotaxis (Procko and McColl, 2005; Van Haastert and Devreotes, 2004). PI3K will play a crucial role in both sensing the ATP gradient and determining the cell polarity of the microglia.

Akt is activated through binding of its PH domains to lipid products of PI3K on the plasma membrane (Scheid and Woodgett, 2003). In this study ATP-induced increase in Akt phosphorylation was suppressed by pretreatment with a P2Y$_{12}$R antagonist or PI3K inhibitors (Fig. 3). These findings indicated that Akt is phosphorylated following PI3K activation downstream of P2Y$_{12}$R in microglia. Interestingly, the increase in the Akt phosphorylation was suppressed by chelation of extracellular calcium with EGTA (Fig. 4), and depletion of intracellular calcium by BAPTA-AM also blocked the Akt phosphorylation (data not shown). These results indicate that activation of the PI3K-Akt signal pathway is regulated by an increase in $[Ca^{2+}]_i$. Previous studies have shown that in some cells an increase in $[Ca^{2+}]_i$ can activate Akt through PI3K-dependent or independent pathways. An increase in $[Ca^{2+}]_i$ can also activate Src or proline-rich/Ca^{2+}-activated tyrosine kinase Pyk2, thereby directly or indirectly regulating the PI3K activation (Chen et al., 2001; Gendron et al., 2003; Okuda et al., 1999). Protein kinase C (PKC) or Ca^{2+}/calmodulin-dependent protein kinase which is activated by calcium, lies upstream of Akt or directly phosphorylates Akt (Bauer et al., 2003; Gliki et al., 2002; Tanaka et al., 2003; Yano et al., 1998). Further investigation is needed to determine how the calcium signaling regulates the PI3K/Akt activation in microglia.

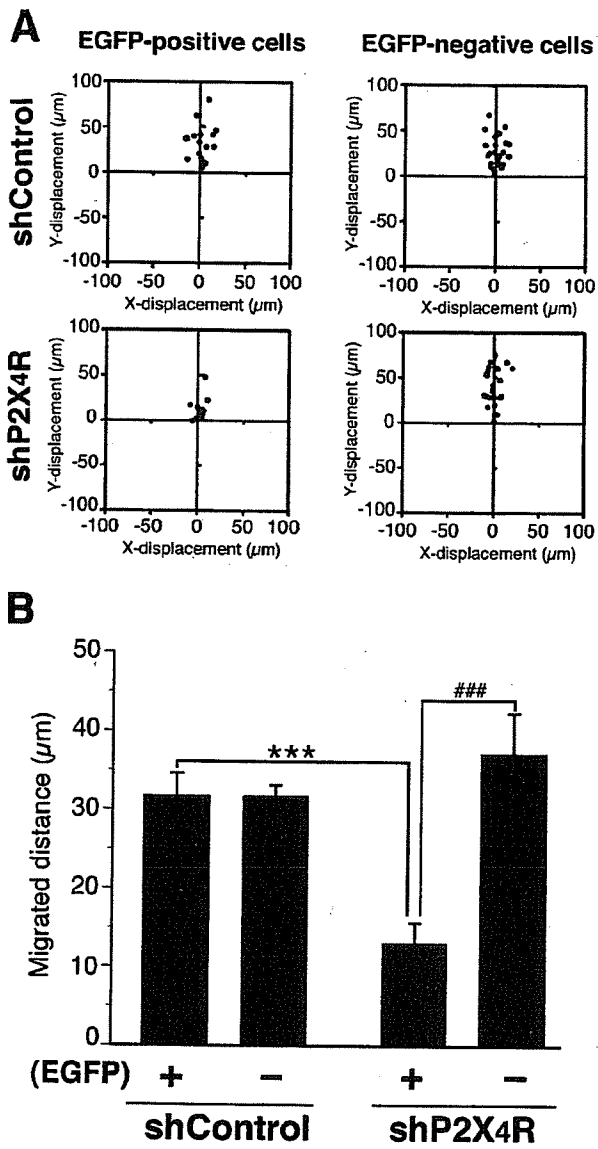

Fig. 10. Inhibitory effect of $P2X_4R$ downregulation on ATP-induced microglial chemotaxis. (**A**) Microglia were transduced with the lentivirus vectors and microglial migration towards 50 μM ATP was observed in the Dunn chemotaxis chamber. The distance and direction of movement by individual cells are shown as x and y coordinates on scatter diagrams. (**B**) Each chemotaxis was quantified by measuring the (x, y) distance migrated from the starting position of cells. Data are means ± SD of three independent experiments. $^{***}P < 0.001$, Student's t-test, compared with shControl EGFP-positive cells; $^{###}P < 0.001$, compared with shP2X4R EGFP-negative cells.

The ATP-induced increase in $[Ca^{2+}]_i$ in microglia has been shown to be suppressed by chelation of extracellular calcium or pretreatment with TNP-ATP, but not by PPADS or BBG (Tsuda et al., 2003). The present study showed that shRNA-mediated downregulation of $P2X_4R$ in microglia suppressed the ATP-induced increase in $[Ca^{2+}]_i$ (Fig. 8). These observations suggest that the increase in $[Ca^{2+}]_i$ is mainly caused by the influx of extracellular calcium through $P2X_4R$. ATP-induced PI3K/Akt activation was inhibited by pretreatment with TNP-ATP, but not with PPADS or BBG (Fig. 6). Interference with $P2X_4R$ expression markedly inhibited the ATP-induced microglial chemotaxis (Fig. 10) without affecting membrane ruffling (Fig. 9), the same as the effects of PI3K inhibitors (Figs. 1 and 2). We therefore suspect that the $P2X_4R$-mediated calcium signaling may be involved in PI3K/Akt activation and regulate microglial chemotaxis. Local Ca^{2+} mobilization through $P2X_4R$ at membrane ruffles may be necessary for maintenance or enhancement of the local $P2Y_{12}R$-activated PI3K signals.

Membrane ruffling is generated by dynamic remodeling of the actin cytoskeleton at the plasma membrane and is thought to be a crucial process for cell migration (Small et al., 2002). $P2Y_{12}R$ activation is essential for ATP-induced membrane ruffling and triggers intracellular signaling events that lead to microglial chemotaxis toward ATP. Ca^{2+} imaging showed that shP2×4R did not completely suppress the ATP-evoked increase in $[Ca^{2+}]_i$ (Fig. 9), suggesting that other subtypes of ATP receptor are involved in the Ca^{2+} response. P2Y receptors are generally linked to activation of phospholipase C (PLC) that catalyzes the hydrolysis of phosphatidylinositol 4,5-bisphosphate to the intracellular messenger inositol 1,4,5, triphosphate (IP_3) and diacylglycerol (Communi et al., 2000). ATP-stimulated $P2Y_{12}R$ will induce PLC activation, leading to IP_3-mediated Ca^{2+} release from intracellular calcium stores in microglia. P2Y receptors modulate G-protein coupled or voltage-dependent ion channels that affect the Ca^{2+} current (Van Kolen and Slegers, 2006). Vial et al. (2002) reported that coactivation of $P2X_1R$ and $P2Y_1R$ in platelets synergistically enhances the Ca^{2+} response and suggested that $P2X_1$ may have a priming role in the activation of $P2Y_1R$ during platelet activation. Further study is needed to analyze cross-talk between $P2X_4R$ and other signal pathways downstream of $P2Y_{12}R$, such as the adenylate cyclase pathway or PLC pathway.

$P2Y_{12}R$ is constitutively expressed in microglia in the normal brain (Sasaki et al., 2003). A recent report by Haynes et al. (2006) shows that $P2Y_{12}R$ is essential for early microglial responses towards either a local ATP injection or a focal laser injury in brain slices. $P2Y_{12}R$ play crucial roles in regulating the morphological changes in ramified microglia and cell migration by activated microglia in response to ATP released by surrounding cells and its hydrolysis product ADP. By contrast, $P2X_4R$ expression in microglia is lower in the normal brain and spinal cord, and it is significantly upregulated in activated microglia within 24 h after ischemia or nerve injury (Cavaliere et al., 2003; Schwab et al., 2005; Zhang et al., 2006). Tsuda et al. (2003) recently reported that the $P2X_4R$ expression is induced in spinal microglia during the tactile allodynia observed after nerve injury. These observations together with our own findings suggest that $P2X_4R$ activation may modulate or enhance the microglial cell migration in pathological conditions. Although further study is needed to clarify the molecular mechanisms underlying the microglial cell migration

mediated by P2Y$_{12}$R and P2X$_4$R, the findings in the present study may contribute to understanding the ATP-induced changes in microglial dynamics in the brain in normal and pathological states.

ACKNOWLEDGMENTS

We thank Dr. Miyoshi (Bio Resource Center, RIKEN, Tsukuba, Japan) for providing us with lentivirus vector system, and Dr. Shin'ichi Takeda, Dr. Hirohiko Hojoh, and Mr. Masuda Satoshi (National Institute of Neuroscience) for their advice and technical support.

REFERENCES

Bauer B, Jenny M, Fresser F, Uberall F, Baier G. 2003. AKT1/PKBα is recruited to lipid rafts and activated downstream of PKC isotypes in CD3-induced T cell signaling. FEBS Lett 541:155–162.

Bellacosa A, Testa JR, Staal SP, Tsichlis PN. 1991. A retroviral oncogene, akt, encoding a serine–threonine kinase containing an SH2-like region. Science 254:274–277.

Cavaliere F, Florenzano F, Amadio S, Fusco FR, Viscomi MT, D'Ambrosi N, Vacca F, Sancesario G, Bernardi G, Molinari M, Volonte C. 2003. Up-regulation of P2X$_2$, P2X$_4$ receptor and ischemic cell death: Prevention by P2 antagonists. Neuroscience 120:85–98.

Chen R, Kim O, Yang J, Sato K, Eisenmann KM, McCarthy J, Chen H, Qiu Y. 2001. Regulation of Akt/PKB activation by tyrosine phosphorylation. J Biol Chem 276:31858–31862.

Comalada M, Xaus J, Sanchez E, Valledor AF, Celada A. 2004. Macrophage colony-stimulating factor-, granulocyte–macrophage colony-stimulating factor-, or IL-3-dependent survival of macrophages, but not proliferation, requires the expression of p21(Waf1) through the phosphatidylinositol 3-kinase/Akt pathway. Eur J Immunol 34:2257–2267.

Communi D, Janssens R, Suarez-Huerta N, Robaye B, Boeynaems JM. 2000. Advances in signalling by extracellular nucleotides. The role and transduction mechanisms of P2Y receptors. Cell Signal 12:351–360.

Czajkowski R, Banachewicz W, Ilnytska O, Drobot LB, Baranska J. 2004. Differential effects of P2Y$_1$ and P2Y$_{12}$ nucleotide receptors on ERK1/ERK2 and phosphatidylinositol 3-kinase signalling and cell proliferation in serum-deprived and nonstarved glioma C6 cells. Br J Pharmacol 141:497–507.

Davalos D, Grutzendler J, Yang G, Kim JV, Zuo Y, Jung S, Littman DR, Dustin ML, Gan WB. 2005. ATP mediates rapid microglial response to local brain injury in vivo. Nat Neurosci 8:752–758.

Ferrari D, Villalba M, Chiozzi P, Falzoni S, Ricciardi-Castagnoli P, Di Virgilio F. 1996. Mouse microglial cells express a plasma membrane pore gated by extracellular ATP. J Immunol 156:1531–1539.

Gendron FP, Neary JT, Theiss PM, Sun GY, Gonzalez FA, Weisman GA. 2003. Mechanisms of P2X$_7$ receptor-mediated ERK1/2 phosphorylation in human astrocytoma cells. Am J Physiol Cell Physiol 284: C571–C581.

Gliki G, Wheeler-Jones C, Zachary I. 2002. Vascular endothelial growth factor induces protein kinase C (PKC)-dependent Akt/PKB activation and phosphatidylinositol 3′-kinase-mediates PKC δ phosphorylation: Role of PKC in angiogenesis. Cell Biol Int 26:751–759.

Haynes SE, Hollopeter G, Yang G, Kurpius D, Dailey ME, Gan WB, Julius D. 2006. The P2Y(12) receptor regulates microglial activation by extracellular nucleotides. Nat Neurosci 12:1512–1519.

Honda S, Sasaki Y, Ohsawa K, Imai Y, Nakamura Y, Inoue K, Kohsaka S. 2001. Extracellular ATP or ADP induce chemotaxis of cultured microglia through Gi/o-coupled P2Y receptors. J Neurosci 21:1975–1982.

Illes P, Alexandre Ribeiro J. 2004. Molecular physiology of P2 receptors in the central nervous system. Eur J Pharmacol 483:5–17.

Imai Y, Ibata I, Ito D, Ohsawa K, Kohsaka S. 1996. A novel gene iba1 in the major histocompatibility complex class III region encoding an EF hand protein expressed in a monocytic lineage. Biochem Biophys Res Commun 224:855–862.

Inoue K. 2002. Microglial activation by purines and pyrimidines. Glia 40:156–163.

Inoue K, Nakajima K, Morimoto T, Kikuchi Y, Koizumi S, Illes P, Kohsaka S. 1998. ATP stimulation of Ca^{2+}-dependent plasminogen release from cultured microglia. Br J Pharmacol 123:1304–1310.

Ito D, Imai Y, Ohsawa K, Nakajima K, Fukuuchi Y, Kohsaka S. 1998. Microglia-specific localisation of a novel calcium binding protein, Iba1. Brain Res Mol Brain Res 57:1–9.

James G, Butt AM. 2002. P2Y and P2X purinoceptor mediated Ca^{2+} signalling in glial cell pathology in the central nervous system. Eur J Pharmacol 447:247–260.

Kreutzberg GW. 1996. Microglia: A sensor for pathological events in the CNS. Trends Neurosci 19:312–318.

Moran LB, Graeber MB. 2004. The facial nerve axotomy model. Brain Res Brain Res Rev 44:154–178.

Nakajima K, Kohsaka S. 2005.Response of microglia to brain injury. In: Kettenmann H, Ransom BR, editors. Neuroglia. New York: Oxford University Press. pp 443–453.

Nakajima K, Shimojo M, Hamanoue M, Ishiura S, Sugita H, Kohsaka S. 1992. Identification of elastase as a secretory protease from cultured rat microglia. J Neurochem 58:1401–1408.

Nasu-Tada K, Koizumi S, Inoue K. 2005. Involvement of β1 integrin in microglial chemotaxis and proliferation on fibronectin: Different regulations by ADP through PKA. Glia 52:98–107.

Nimmerjahn A, Kirchhoff F, Helmchen F. 2005. Resting microglial cells are highly dynamic surveillants of brain parenchyma in vivo. Science 308:1314–1318.

Nishitsuji H, Ikeda T, Miyoshi H, Ohashi T, Kannagi M, Masuda T. 2004. Expression of small hairpin RNA by lentivirus-based vector confers efficient and stable gene-suppression of HIV-1 on human cells including primary non-dividing cells. Microbes Infect 6: 76–85.

Nörenberg W, Langosch JM, Gebicke-Haerter PJ, Illes P. 1994. Characterization and possible function of adenosine 5′-triphosphate receptors in activated rat microglia. Br J Pharmacol 111:942–950.

Okuda M, Takahashi M, Suero J, Murry CE, Traub O, Kawakatsu H, Berk BC. 1999. Shear stress stimulation of p130(cas) tyrosine phosphorylation requires calcium-dependent c-Src activation. J Biol Chem 274:26803–26809.

Procko E, McColl SR. 2005. Leukocytes on the move with phosphoinositide 3-kinase and its downstream effectors. Bioessays 27:153–163.

Ralevic V, Burnstock G. 1998. Receptors for purines and pyrimidines. Pharmacol Rev 50:413–492.

Ridley AJ. 2001. Rho proteins, PI 3-kinases, and monocyte/macrophage motility. FEBS Lett 498:168–171.

Sasaki Y, Hoshi M, Akazawa C, Nakamura Y, Tsuzuki H, Inoue K, Kohsaka S. 2003. Selective expression of Gi/o-coupled ATP receptor P2Y$_{12}$ in microglia in rat brain. Glia 44:242–250.

Scheid MP, Woodgett JR. 2003. Unravelling the activation mechanisms of protein kinase B/Akt. FEBS Lett 546:108–112.

Schwab JM, Guo L, Schluesener HJ. 2005. Spinal cord injury induces early and persistent lesional P2X$_4$ receptor expression. J Neuroimmunol 163:185–189.

Small JV, Stradal T, Vignal E, Rottner K. 2002. The lamellipodium: Where motility begins. Trends Cell Biol 12:112–120.

Soulet C, Sauzeau V, Plantavid M, Herbert JM, Pacaud P, Payrastre B, Savi P. 2004. Gi-dependent and -independent mechanisms downstream of the P2Y$_{12}$ ADP-receptor. J Thromb Haemost 2:135–146.

Stence N, Waite M, Dailey ME. 2001. Dynamics of microglial activation: A confocal time-lapse analysis in hippocampal slices. Glia 33:256–266.

Streit WJ. 2002. Microglia as neuroprotective, immunocompetent cells of the CNS. Glia 40:133–139.

Tanaka Y, Gavrielides MV, Mitsuuchi Y, Fujii T, Kazanietz MG. 2003. Protein kinase C promotes apoptosis in LNCaP prostate cancer cells through activation of p38 MAPK and inhibition of the Akt survival pathway. J Biol Chem 278:33753–33762.

Tsuda M, Shigemoto-Mogami Y, Koizumi S, Mizokoshi A, Kohsaka S, Salter MW, Inoue K. 2003. P2X$_4$ receptors induced in spinal microglia gate tactile allodynia after nerve injury. Nature 424:778–783.

Van Haastert PJ, Devreotes PN. 2004. Chemotaxis: Signalling the way forward. Nat Rev Mol Cell Biol 5:626–634.

Vanhaesebroeck B, Leevers SJ, Ahmadi K, Timms J, Katso R, Driscoll PC, Woscholski R, Parker PJ, Waterfield MD. 2001. Synthesis and function of 3-phosphorylated inositol lipids. Annu Rev Biochem 70:535–602.

Van Kolen K, Slegers H. 2004. P2Y$_{12}$ receptor stimulation inhibits β-adrenergic receptor-induced differentiation by reversing the cyclic AMP-dependent inhibition of protein kinase B. J Neurochem 89:442–453.

Van Kolen K, Slegers H. 2006. Integration of P2Y receptor-activated signal transduction pathways in G protein-dependent signaling networks. Purinergic Signalling 2:451–469.

Vial C, Rolf MG, Mahaut-Smith MP, Evans RJ. 2002. A study of P2X1 receptor function in murine megakaryocytes and human platelets reveals synergy with P2Y receptors. Br J Pharmacol 135:363–372.

Verkhratsky A, Kettenmann H. 1996. Calcium signalling in glial cells. Trends Neurosci 19:346–352.

Walz W, Ilschner S, Ohlemeyer C, Banati R, Kettenmann H. 1993. Extracellular ATP activates a cation conductance and a K^+ conductance in cultured microglial cells from mouse brain. J Neurosci 13:4403–4411.

Webb SE, Pollard JW, Jones GE. 1996. Direct observation and quantification of macrophage chemoattraction to the growth factor CSF-1. J Cell Sci 109:793–803.

Weiss-Haljiti C, Pasquali C, Ji H, Gillieron C, Chabert C, Curchod ML, Hirsch E, Ridley AJ, van Huijsduijnen RH, Camps M, Rommel C. 2004. Involvement of phosphoinositides 3-kinase γ, Rac, and PAK signaling in chemokine-induced macrophage migration. J Biol Chem 279:43273–43284.

Xiang Z, Burnstock G. 2005. Expression of P2X receptors on rat microglial cells during early development. Glia 52:119–126.

Yano S, Tokumitsu H, Soderling TR. 1998. Calcium promotes cell survival through CaM-K kinase activation of the protein-kinase-B pathway. Nature 396:584–587.

Yogosawa S, Hatakeyama S, Nakayama KI, Miyoshi H, Kohsaka S, Akazawa C. 2005. Ubiquitylation and degradation of serum-inducible kinase by hVPS18, a RING-H2 type ubiquitin ligase. J Biol Chem 280: 41619–41627.

Zhang Z, Artelt M, Burnet M, Trautmann K, Schluesener HJ. 2006. Lesional accumulation of $P2X_4$ receptor monocytes following experimental traumatic brain injury. Exp Neurol 197:252–257.

Three-dimensional reconstruction of the membrane skeleton at the plasma membrane interface by electron tomography

Nobuhiro Morone,[1,2,3] Takahiro Fujiwara,[4] Kotono Murase,[1] Rinshi S. Kasai,[4] Hiroshi Ike,[1] Shigeki Yuasa,[3] Jiro Usukura,[2] and Akihiro Kusumi[1,4]

[1]Kusumi Membrane Organizer Project, Exploratory Research for Advanced Technology (ERATO), Japan Science and Technology Agency, Nagoya 460-0012, Japan
[2]Department of Cell Biology and Anatomy, Graduate School of Medicine, Nagoya University, Nagoya 466-8550, Japan
[3]Department of Ultrastructural Research, National Institute of Neuroscience, National Center of Neurology and Psychiatry, Tokyo 187-8502, Japan
[4]Membrane Mechanisms Project, International Cooperative Research Project (ICORP), Japan Science and Technology Agency, Institute for Frontier Medical Sciences, Kyoto University, Shougoin, Kyoto 606-8507, Japan

Three-dimensional images of the undercoat structure on the cytoplasmic surface of the upper cell membrane of normal rat kidney fibroblast (NRK) cells and fetal rat skin keratinocytes were reconstructed by electron tomography, with 0.85-nm–thick consecutive sections made ~100 nm from the cytoplasmic surface using rapidly frozen, deeply etched, platinum-replicated plasma membranes. The membrane skeleton (MSK) primarily consists of actin filaments and associated proteins. The MSK covers the entire cytoplasmic surface and is closely linked to clathrin-coated pits and caveolae. The actin filaments that are closely apposed to the cytoplasmic surface of the plasma membrane (within 10.2 nm) are likely to form the boundaries of the membrane compartments responsible for the temporary confinement of membrane molecules, thus partitioning the plasma membrane with regard to their lateral diffusion. The distribution of the MSK mesh size as determined by electron tomography and that of the compartment size as determined from high speed single-particle tracking of phospholipid diffusion agree well in both cell types, supporting the MSK fence and MSK-anchored protein picket models.

Introduction

The portion of the cytoskeleton that is closely associated with the cytoplasmic surface of the plasma membrane is often called the membrane skeleton (MSK; Heuser and Kirschner, 1980; Hirokawa and Heuser, 1981; Bennett, 1990; Luna and Hitt, 1992). The term MSK is useful partly because this part of the cytoskeleton is expected to differ from the bulk cytoskeleton in terms of its structure and protein composition, for its interactions with the plasma membrane in general and with specific molecules in the plasma membrane, and also because it plays important roles in a variety of membrane functions. It is involved in the localization of transmembrane proteins at specific sites in the cell membrane (Bennett and Chen, 2001; Pan et al., 2006) and in endocytosis and exocytosis (Gaidarov et al., 1999; Valentijn et al., 2000) in various cell types. It also provides the plasma membrane with the mechanical strength and resilience to withstand the stress and shear forces from the outside environment, which is well established in the thick cortical actin layers in immune cells (Hartwig and Yin, 1988) and in the spectrin–actin network in red blood cells (Mohandas and Evans, 1994; Discher et al., 1995). Therefore, the MSK works as a part of the plasma membrane as well as a part of the cytoskeleton. It is a truly interfacial structure between the bulk cytoskeleton and the 2D bilayer of the plasma membrane.

Recently, a new function of the MSK has become apparent. It was proposed that a part of the MSK is directly and closely associated with the cytoplasmic surface of the plasma membrane, and this part induces partitioning of the cell membrane with regard to the translational diffusion of membrane molecules based on high speed single-particle tracking data on membrane proteins and lipids (Jacobson et al., 1995; Kusumi et al., 2005). In the short-time regime, these membrane molecules are temporarily confined within the compartments delimited by the MSK mesh, and, in the long-time regime, they undergo macroscopic diffusion by hopping between these compartments (MSK fence model). In the fence model, as a result of the collision of the cytoplasmic domains of transmembrane

Correspondence to Akihiro Kusumi: akusumi@frontier.kyoto-u.ac.jp

Abbreviations used in this paper: CCP, clathrin-coated pit; FRSK, fetal rat skin keratinocyte; MSK, membrane skeleton; NRK, normal rat kidney fibroblast.

The online version of this article contains supplemental material.

The Journal of Cell Biology, Vol. 174, No. 6, September 11, 2006 851–862
http://www.jcb.org/cgi/doi/10.1083/jcb.200606007

Supplemental Material can be found at:
http://www.jcb.org/cgi/content/full/jcb.200606007/DC1

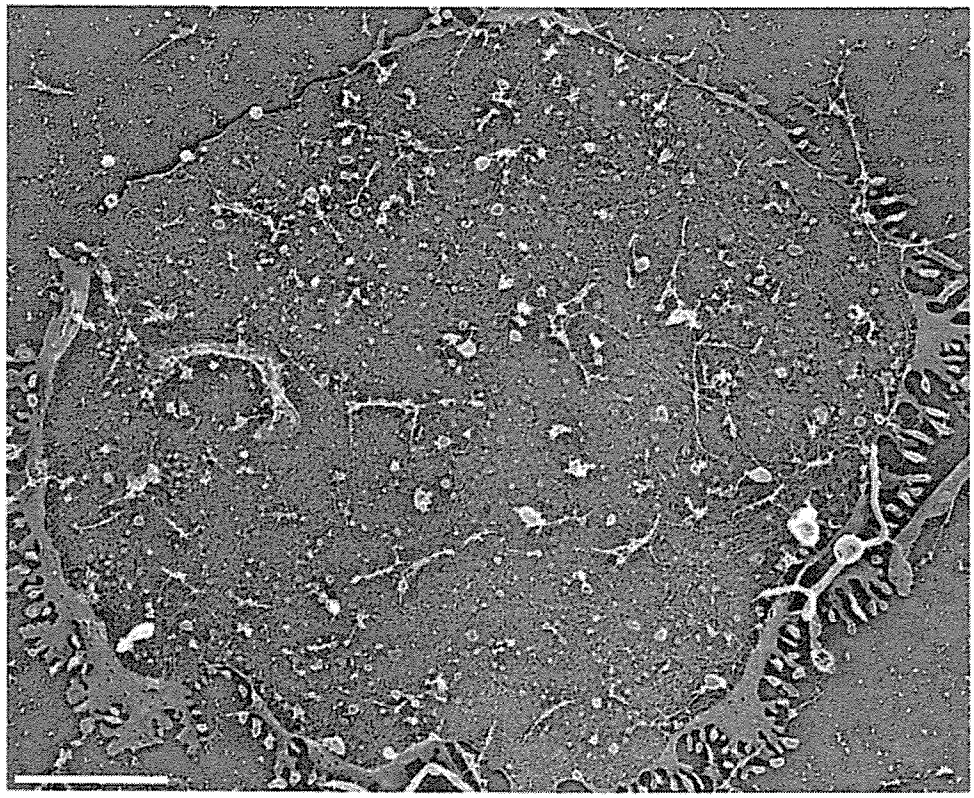

Figure 1. **A bird's-eye view of the large cytoplasmic surface of the upper cell membrane (the membrane facing the buffer rather than the coverslip) of an NRK cell observed by rapid-freeze, deep-etch, freeze-replica EM.** Bar, 2.5 μm.

proteins with the MSK, transmembrane proteins are temporarily confined in the MSK mesh (Sheetz, 1983; Tsuji and Ohnishi, 1986; Tsuji et al., 1988; Saxton, 1989, 1990; Sako and Kusumi, 1994, 1995; Jacobson et al., 1995; Kusumi and Sako, 1996; Saxton and Jacobson, 1997; Sako et al., 1998; Tomishige et al., 1998; Suzuki et al., 2005).

Lipid molecules also undergo hop diffusion, which might be explained by the anchored protein picket model (Fujiwara et al., 2002; Murase et al., 2004; Kusumi et al., 2005). In this model, various transmembrane proteins anchored to the actin-based MSK might effectively act as rows of pickets against the free diffusion of all of the molecules incorporated in the cell membrane as a result of steric hindrance and circumferential slowing (a hydrodynamic frictionlike effect, which propagates quite far from the immobile protein surface; without this effect, pickets will not be effective for blocking diffusion; Bussell et al., 1994, 1995) of the immobile picket proteins anchored to and lined up along the MSK. Lipid movement is affected only by pickets, whereas both pickets and fences would act on transmembrane proteins. These MSK picket-fence effects would be dramatically enhanced when the membrane receptor molecules form signaling complexes upon ligand binding as a result of receptor oligomerization and/or binding of the cytoplasmic signaling molecules to the receptor, leading to the trapping of signaling complexes in the MSK mesh, where the extracellular signal is received. This would enable spatial confinement and regulation of the downstream signaling events (Kusumi and Sako, 1996; Iino et al., 2001).

Despite the importance of the MSK functions and the long history of its study using EM (Byers and Porter, 1977; Heuser and Kirschner, 1980; Hirokawa and Heuser, 1981; Heuser and Anderson, 1989; Hartwig and DeSisto, 1991; Rothberg et al., 1992), our knowledge of its structure and the overall distribution over the plasma membrane has been very limited. For example, we do not know whether the MSK exists everywhere on the cytoplasmic surface of the cell membrane, how extensive the spatial variations of MSK mesh size is, and whether and how MSK interacts with other structures in the plasma membrane such as clathrin-coated pits (CCPs), caveolae, and cell adhesion structures. Even the structure of the MSK of the human red blood cell ghost, a traditional paradigm for MSK studies, is not satisfactorily understood (Sheetz and Sawyer, 1978; Tsukita et al., 1980; Branton et al., 1981; Shen et al., 1986; Ursitti et al., 1991; Takeuchi et al., 1998).

In this study, to further advance our understanding of the MSK structure and function, we observed the undercoat structure on the cytoplasmic surface of the plasma membrane of cultured mammalian cells using rapid-freeze, deep-etch, immunoreplication EM. We paid special attention to the following three points.

First, we tried to consistently prepare and observe large plasma membrane fragments (>10 μm in diameter) to facilitate inspections of very large plasma membrane areas. Almost all of

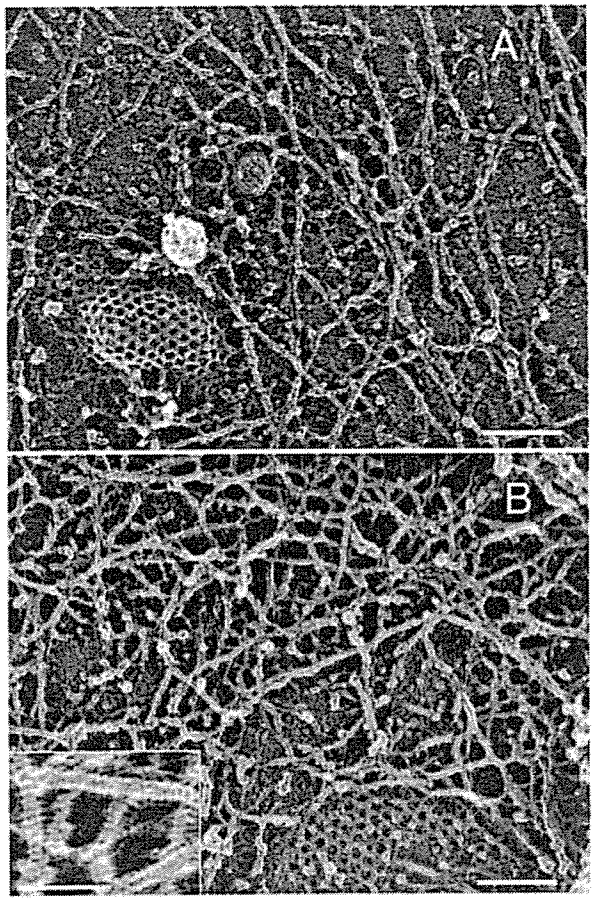

Figure 2. **Magnified MSK images of an NRK and FRSK cell on the cytoplasmic surface of the upper membrane.** (A) NRK cell; (B) FRSK cell. Clathrin-coated structures (A and B) and a caveola (A) show the cytoplasmic surface. The striped banding patterns with the 5.5-nm periodicity on individual filaments are characteristic of actin filaments. These images also reveal close links of the MSK actin filaments with the clathrin-coated structures and caveolae. Bars (A and B), 100 nm; (inset) 50 nm.

the previous MSK studies, including those cited above, investigated the ultrastructural features of the structure of interest, but within a very limited view field. By observing these large membrane surfaces, the spatial variations of the MSK mesh size and of the number density of CCPs and caveolae can be reliably examined.

Second, the 3D reconstruction of the undercoat structure within 100 nm from the cytoplasmic surface of the plasma membrane was performed using electron tomography for the platinum-replicated samples: 97–141 images for a specimen tilted at different angles (every 1°) with respect to the incident electron beam in the range of ±48–70° were obtained and then converted to 100–121 sliced images of every 0.85–1.34 nm for the 3D reconstructed images (Perkins et al., 1997; Medalia et al., 2002; Lucic et al., 2005; McIntosh et al., 2005; Zeuschner et al., 2006).

Third, using the 3D reconstructed images of the MSK structure within 13.6 nm (16 slices of 0.85-nm thickness) from the cytoplasmic surface, the MSK mesh size distribution on the cytoplasmic surface of the plasma membrane was determined. This part of the MSK, which is closely associated with the cytoplasmic surface of the plasma membrane, might form the compartment boundaries for partitioning of the plasma membrane for the diffusion of membrane molecules, thus determining the compartment size. Therefore, it is interesting to compare the distribution of the MSK mesh size on the membrane determined this way and that of the compartment size sensed by membrane molecules. Because the compartment size distributions for membrane molecules are very different between normal rat kidney fibroblast (NRK; median = 230 nm) and fetal rat skin keratinocyte (FRSK; median = 41 nm) cell lines (Fujiwara et al., 2002; Murase et al., 2004), the distribution of the MSK mesh size on the membrane surface was examined using these two cell lines. Although the compartment size is very different between these cell lines, within each cell type, the histogram for the MSK mesh size on the membrane surface is very similar to that for the diffusion compartment size. This strongly supports the MSK fence and MSK-anchored transmembrane protein picket models.

Results

Bird's-eye view of the undercoat structure of the upper cell membrane

Glass coverslips precationized by a treatment with Alcian blue were placed on top of the cells cultured in 35-mm plastic dishes and were allowed to settle and attach to the upper cell membrane at 4°C for 15 min. The buffer containing 1% PFA and 0.25% glutaraldehyde was then added to the space between the coverslip and the plastic bottom of the culture dish. As the coverslip was floated apart, the cells were ruptured and the upper cell membrane was retained, still adhering to the overlaying Alcian blue–coated coverslip. The upper membrane was rapidly frozen by pressing its exposed cytoplasmic surface onto a pure copper block precooled by liquid helium. The frozen sample was deep etched, coated with platinum-carbon, and observed under an electron microscope. We have made extensive efforts to reproducibly prepare and observe large cell membrane fragments >10 μm in diameter.

Fig. 1 is a typical electron micrograph providing a bird's-eye view of the cytoplasmic surface of a large area of the upper cell membrane of a cultured NRK cell. Many such EM images showing the cytoplasmic surfaces of large cell membrane fragments were obtained for NRK and FRSK cells, suggesting that the entire (upper) plasma membrane, except for the places where CCPs and caveolae exist, is coated with the filamentous netlike structure.

Fig. 2 (A and B), which was obtained for an NRK cell (Fig. 2 A) and an FRSK cell (Fig. 2 B), shows the magnified images of the cytoplasmic surface of the plasma membrane, exhibiting extensive filamentous netlike structures, which are the MSK. The presence of clathrin-coated structures shows that this is indeed the cytoplasmic surface. The striped banding patterns with a 5.5-nm periodicity on individual filaments are characteristic of actin filaments and, thus, indicate that these are actin filaments (Heuser and Kirschner, 1980; Heuser, 1983; Katayama,

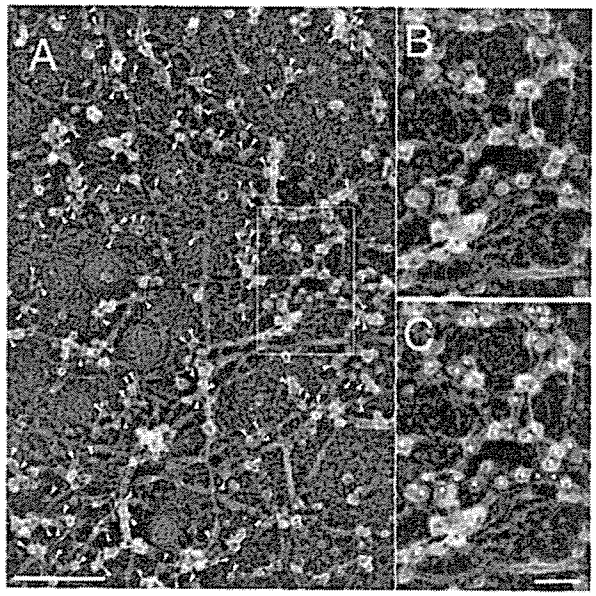

Figure 3. **Immunogold labeling also indicates that the major component of MSK is actin filaments (NRK cell).** Actin filaments were indirectly immunolabeled with 5-nm colloidal gold particles coated with secondary antibodies. Each gold particle can be identified as a clear white spot (colloidal gold particle) surrounded by a fuzzy gray ring, which is caused by the platinum rotary shadowing around the secondary antibody coating of the gold particle. Representative probe images are indicated by arrowheads. (A) Most of the filamentous structures are labeled by colloidal gold probes. (B and C) The boxed area in A is shown at a higher magnification. In C, the gold particles are marked by yellow dots. The filaments with the 5.5-nm striped banding pattern, which is characteristic of the actin filament, are labeled with these gold probes. Bars (A), 200 nm; (B and C) 50 nm.

1998; Schoenenberger et al., 1999). Because almost all of these filaments contain this striped pattern, it is concluded that the MSK is predominantly composed of actin filaments. This was also confirmed by immunogold staining (see Fig. 3 and related text).

The electron micrograph shown in the inset in Fig. 2 B indicates the spatial resolution: because each band in the striped pattern with a 5.5-nm periodicity is visibly separated, the effective resolution is thought to be ~2 nm (both the thickness of the platinum coating and the platinum granule size are ≤2 nm; Heuser and Kirschner, 1980; Heuser, 1983). The MSK structure observed here on the upper cell membrane is similar to that on the bottom cell membrane (the part of the cell membrane facing the coverslip) observed previously (Heuser and Anderson, 1989).

These results suggest that the cytoplasmic surface of a portion of the upper cell membrane >10 μm in diameter was visualized with a spatial resolution of ~2 nm, which is much smaller than the width of a single actin filament or the repeat distance of the stripes. As shown in Figs. 1 and 2 (A and B), the MSK is likely to cover the entire cytoplasmic surface of the upper cell membrane except for the places where CCPs and caveolae are present in both NRK and FRSK cells. Such a notion of the complete coverage of the cytoplasmic surface of the plasma membrane by actin filaments might have existed for >30 yr in a part of the EM community (Byers and Porter, 1977; for review see Sheetz et al., 2006), but the data specifically indicating that the actin filaments of the MSK may cover the entire cell membrane has not been presented in the literature, as done here, nor shared in the cell biology community. The EM observations shown in this study are consistent with the MSK fence and anchored transmembrane protein picket models, in which the entire plasma membrane except for the specific membrane domains is partitioned into many small compartments with regard to lateral diffusion of the molecules incorporated in the plasma membrane.

The MSK predominantly consists of actin filaments: immunogold labeling of actin and actin-binding proteins

To further examine whether the MSK is predominantly composed of actin filaments (and partly because the 5.5-nm periodicity of the banding pattern is somewhat difficult to discern in some of the filaments), we examined it using an indirect immunolabeling method with 5-nm-diameter colloidal gold particles (see Materials and methods; Fig. 3). On the filaments with striped patterns, the enlarged images (Fig. 3, B and C) show the presence of many colloidal gold actin probes, which appear as distinct white spots surrounded by somewhat blurred white halos, reflecting the platinum shadow over the antibody molecules attached to the gold particle. The electron micrographs in Fig. 3 revealed that almost all of the colloidal gold probes are bound to the filaments located on the cytoplasmic surface (yellow dots). Therefore, it is concluded that actin is the main constituent molecule of the MSK.

Electron tomography of the undercoat structure on the cytoplasmic surface of the plasma membrane

The 3D structure of the undercoat within 100–134 nm from the cytoplasmic surface of the plasma membrane, which includes CCPs, caveolae, and the actin-based MSK, was reconstructed using electron tomography for the platinum-replicated samples. Based on the 97–141 tilt images acquired in the range of ±48–70° every 1° step for a single EM view field, 100–121 sliced images of every 0.85–1.34 nm perpendicular to the z axis (parallel to the image obtained at 0° of the tilt angle) were calculated by a computer (long wavelength [≥~500 nm] undulations of the cell membrane were corrected by the 3D reconstruction software IMOD). The 3D image was reconstructed based on these serial thin slices. Representative images obtained for an EM view field are shown in Video 1 (131 tilt images; an anaglyph produced from images taken at ±12° is shown in Fig. 4 A) and Video 2 (showing the 3D image by rotating the 3D reconstructed undercoat structure; a typical view is shown in Fig. 4 B; videos are available at http://www.jcb.org/cgi/content/full/jcb.200606007/DC1). Throughout the present research, this protocol was used to obtain 3D images.

In these images, because of their 3D representation, it is especially clear that the MSK, which is mostly composed of actin filaments, generally spreads along the membrane, covering almost the entire cytoplasmic surface of the upper membrane except for the places with caveolae and CCPs. In addition,

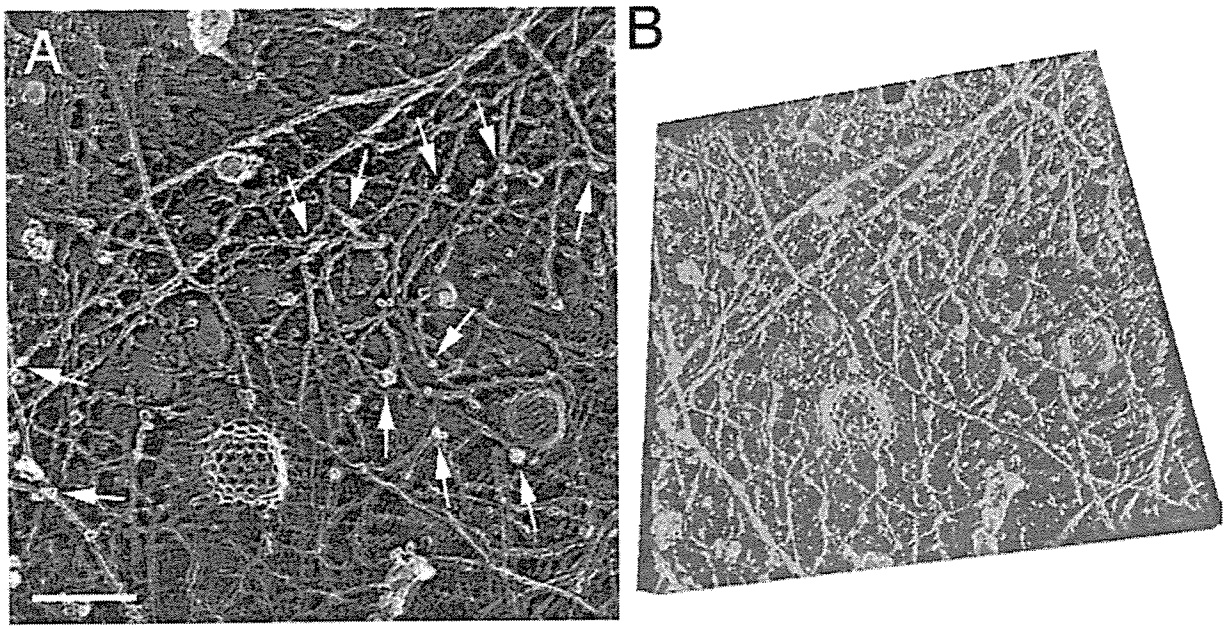

Figure 4. **Stereo electron micrographs and 3D reconstructed images of the undercoat structure, CCPs, and caveolae in NRK cells.** (A) An EM anaglyph of the undercoat structure generated at ±12° of the tilt angle among the 131 tilt images (acquired in the range of ±65° with 1° steps). Use view glasses for the 3D structure (left = red). See Video 1 for all 131 of the tilt images. Arrows indicate actin filaments protruding from the membrane cytoplasmic surface toward the cytoplasm. The arrows point to the places where the protruding actin filaments intersect with the MSK meshwork located close to the membrane. (B) The 3D undercoat structure reconstructed from the tilt images shown in Video 1. See Video 2, where the 3D structure is rotated (available at http://www.jcb.org/cgi/content/full/jcb.200606007/DC1). Bar, 100 nm.

CCPs and caveolae are very closely associated with the actin filaments in the MSK, as seen in these images and also in Figs. 2 (A and B) and 3. These results are consistent with Rothberg et al. (1992), Fujimoto et al. (2000), and Parton (2003), but in NRK cells studied here, many more actin filaments were found to be associated with each CCP or caveola. Furthermore, 92 and 93% of CCPs and caveolae (n = 200) were bound by the actin filaments. These results are consistent with the requirement of filamentous actin for CCP internalization (Qualmann et al., 2000; Merrifield et al., 2002).

Many short, thin filaments protrude toward the cytoplasm, mostly perpendicularly, from the membrane surface (they were short probably because they were broken at the time of the membrane rip off; Fig. 4 A, arrows). Note that these perpendicular filaments are almost always connected to the MSK network lying on the cytoplasmic surface (see the tips of the arrows; Fig. 4 A). Thus, the part of the MSK that is located on the cytoplasmic surface is connected three dimensionally to the cytoskeleton. Together, they will provide mechanical support for the membrane and the force for deforming the membrane.

3D reconstruction of the MSK structure

The part of the actin-based MSK that is in contact with the cytoplasmic surface of the cell membrane has been proposed to partition the cell membrane into 30–230-nm compartments by the fence and picket effect (Edidin et al., 1991; Kusumi and Sako, 1996; Kusumi et al., 2005). If these fence and picket models are correct, the distribution of the mesh size of the MSK on the cytoplasmic surface of the plasma membrane would be practically the same as that of the compartment size determined by diffusion measurements of membrane molecules. To carry out this examination, the 3D reconstruction of MSK by electron tomography provides a unique opportunity because the obtained images provide quantitative data on how far the individual filaments are located from the membrane surface.

In Fig. 5 A, a typical MSK structure quantitatively analyzed in this study is shown in an anaglyph, and its 8.5-nm–thick sections (created by superimposing 10 0.85-nm sections) of the MSK of an NRK cell, starting from the cytoplasmic side toward the membrane, are shown (Fig. 5 B; a series of the original tilt images is shown in Video 3, and a series of sliced images of every 0.85 nm is shown in Video 4, available at http://www.jcb.org/cgi/content/full/jcb.200606007/DC1). The actin-based MSK is visible on image sections 81–110. Individual actin filaments, forming a network as well as bundles, can be identified. Given the high density of the actin filament meshwork, which is much smaller than the optical resolution, conventional fluorescence microscopy will be unable to visualize the MSK meshwork and can visualize only the bundles of actin filaments.

Interface structure of MSK on the cytoplasmic surface of the plasma membrane

The filaments of the MSK that are directly associated with the cytoplasmic surface of the plasma membrane and may be involved in partitioning the plasma membrane were systematically determined. Out of the stack of 121 image slices taken every 0.85 nm from the cytoplasmic surface (~100-nm thick altogether),

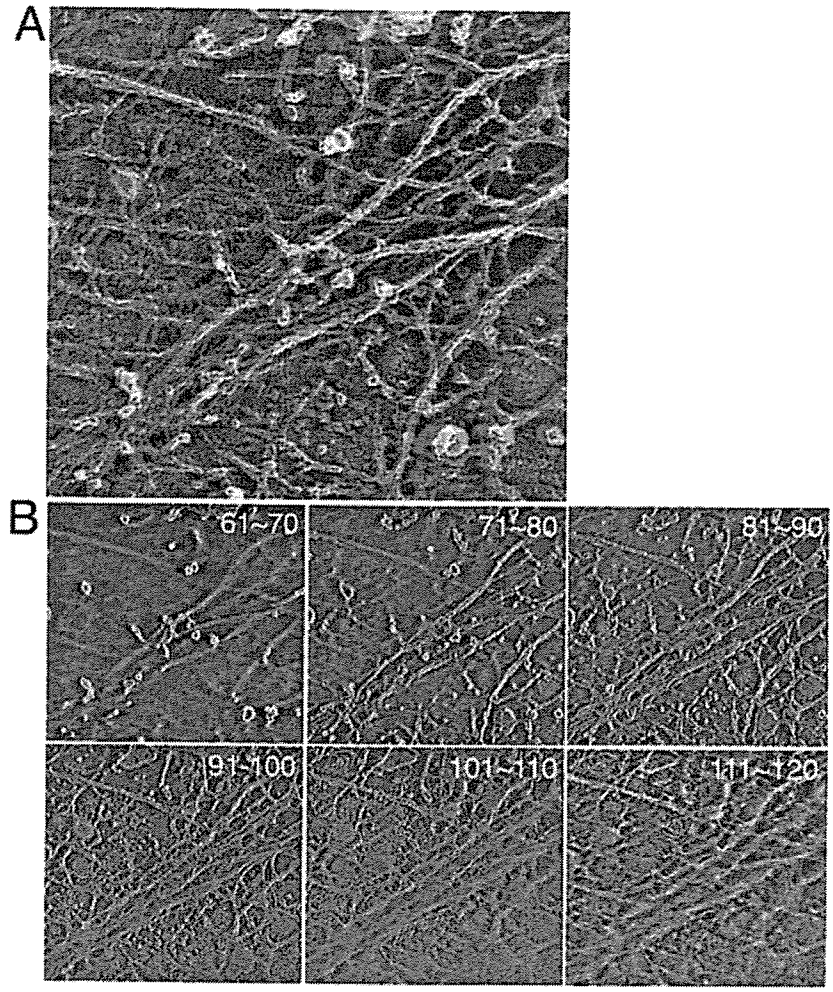

Figure 5. **A series of sliced images of the actin MSK on the plasma membrane cytoplasmic surface of an NRK cell.** (A) A typical actin MSK structure used for analysis of the mesh size on the cytoplasmic surface of the plasma membrane using computed tomography. An anaglyph of the undercoat structure generated at ±12° of the tilt angle among the 97 tilt images (acquired in the range of ±48° with 1° steps). See Video 3 for all 97 of the tilt images. (B) 10 consecutive sections, each 0.85-nm thick, are superimposed, and six of these superimposed images, which represent 60 image sections out of 121 image sections, are shown from the cytoplasmic side toward the plasma membrane side. The numbers here indicate the number of slices counted from the cytoplasmic side. The actin-based MSK near the cytoplasmic surface of the plasma membrane is visible on images 81–110. All 121 of the sliced images of every 0.85 nm are shown in Video 4 (available at http://www.jcb.org/cgi/content/full/jcb.200606007/DC1).

16 consecutive image slices from the membrane surface (~13.6-nm thick altogether) were used for this analysis (Fig. 6, A and B).

In Fig. 6 A (four images on the right) and Fig. 6 B (the second to fourth images), the boxed areas in the left-most images were expanded, and the sections of every 1.7 nm (superposition of two 0.85-nm–thick slices; 330 × 330 nm) are displayed between 0 and 11.9 nm. Using these sections, the filaments that are closely associated with the cytoplasmic surface of the cell membrane were determined. Because the thickness (width in the image) of the actin filament after platinum shadowing is between 9 and 11 nm (consistent with Heuser, 1983) and the thickness of the platinum replica is ≤2 nm (consistent with Heuser, 1983 and Moritz et al., 2000), the height of the actin filament that is associated with the membrane will be 7–9 nm (because the height is given by the actin thickness and one replica thickness, whereas the width in the image is determined by the actin thickness plus two replica thicknesses), with 8 nm being a reasonable estimate. In the series of electron tomography sections shown in Fig. 6 (A and B), the existence of three major classes of filaments with regard to the distance from the membrane surface can be discerned (for details of this analysis, see Materials and methods).

The first class of filaments is distinct in computer-reconstructed sections close to the cytoplasmic surface of the plasma membrane, even in the first ~0–1.7-nm section (because the contrast is reversed in these micrographs, they look more lucent or white), but fade out of the reconstructions 8–10 nm away from the membrane surface (for details, see Materials and methods). These filaments are drawn in green in Fig. 6 C. We interpret that these filaments are in true contact with the plasma membrane (the gap between the filament and the inner membrane surface is <0.85 nm) because they can be seen clearly even in the first 0.85-nm section. These filaments are likely to be the significant ones for generating membrane corrals.

The second class of filaments also looks clear in sections very close to the membrane surface but does not fade out until ~14 nm away from it. We interpret that these may be the actin filaments that had platinum coatings all around their surfaces because they stood off the surface somewhat, which slightly exaggerated their thickness and made them appear as though they were in contact with the plasma membrane when

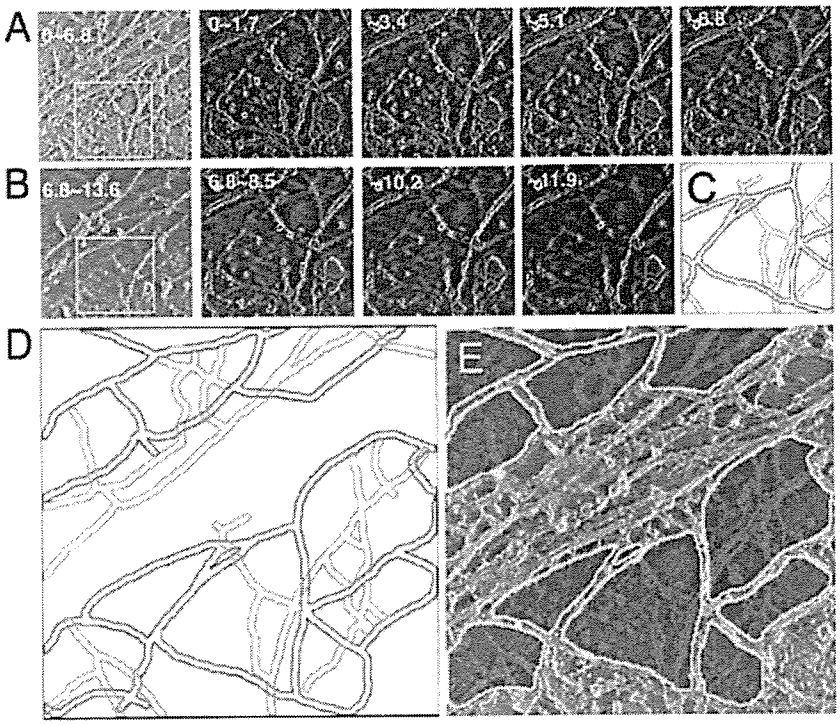

Figure 6. **The method for determining the MSK mesh on the cytoplasmic surface of the plasma membrane, which possibly delimits the compartments of the plasma membrane, using the 3D reconstructed images of the MSK (an NRK cell).** (A and B) The images on the far left are the ~0–6.8- or ~6.8–13.6-nm sections, each of which is a stack of eight 0.85-nm sections of 670 × 670 nm. These are from a series of 121 image sections (0.85-nm thick) from the cytoplasmic surface after the tilt and long wavelength undulation of the cell surface were corrected. The boxed areas in A and B (330 × 330 nm) are expanded on the right of these image stacks, with a section thickness of 1.7 nm (two 0.85-nm sections are superimposed; 330 × 330 nm for each image). (C) The outline of each actin filament adjacent to the membrane surface (green, which could not be observed above 10.2 nm) and that of each actin filament that could be observed above 10.2 nm (red). The same view field and magnification as those for the thinner sections shown in A and B (330 × 330 nm). See Materials and methods for details. (D) The outline of actin filaments in a greater view field, which is the same as those in the thick sections (~0–6.8 and ~6.8–13.6 nm) in A and B (670 × 670 nm, expanded here). (E) The image of the ~0–6.8-nm sections (670 × 670 nm) superimposed by the image of areas surrounded by the filaments outlined in green in D (green areas with yellow outlines). According to the fence and picket models, these areas are likely to be the compartments where membrane molecules are temporarily confined.

in fact they probably were not quite in direct contact. We did not consider these filaments to be close enough to generate membrane corrals.

The third class of filaments is not apparent in sections closest to the plasma membrane but becomes clear some distance away from it (>2–4 nm) and also does not fade out until ~14 nm. We interpret these as being filaments that definitely do not contact the plasma membrane directly and, thus, should not contribute to forming corrals. The second and third classes of filaments are drawn in red in Fig. 6 C.

Therefore, we considered that only the first class of filaments (those drawn in green in Fig. 6, C and D) forms the MSK fences and pickets, and the area surrounded by these filaments is colored green in the 0–6.8-nm section shown in Fig. 6 E. Note that areas are excluded from this analysis in which bundles of actin filaments are present (e.g., the structure crossing diagonally from the bottom left to the top right in Fig. 5), actin filaments are too crowded to be individually discerned, an actin filament is terminated in the middle of a domain (domains that contain a loose end of an actin filament), or CCPs, caveolae, and the smooth surface membrane invaginations are present (the white regions in Fig. 7 C).

Comparison of the MSK mesh size on the plasma membrane determined by electron tomography with the compartment size for the diffusion of membrane molecules

Similar determination of the MSK meshwork was performed for FRSK cells. Representative meshes of the MSK are shown in Fig. 7 (for an FRSK cell, colored to aid in visualization). We performed such analyses for 10 representative stacks of image sections (1,290 × 1,290-nm plane) each for NRK cells and FRSK cells (eight different cell membrane sheets for each cell type) and identified 76 and 1,300 areas bounded by the MSK meshwork, respectively (excluding the regions occupied by stress fibers and other membrane undercoat structures such as CCPs and caveolae; about the same total membrane areas were examined for each cell type, and, thus, the difference in the number of identified areas represents the difference in the area size between these two cell lines). The 2D area size for each domain was measured by Amira software. The distributions of the square root of the area size (the side length, assuming a square shape for the area) for NRK (Fig. 8, pink open bars) and FRSK (blue open bars) cells are shown in Fig. 8. The median values of the area and its square root are 3.9×10^4 nm^2 and 200 nm, respectively, for NRK cells and 2.7×10^3 nm^2 and 52 nm, respectively, for FRSK cells.

The size distributions of the compartments for the diffusion of membrane molecules were obtained for an unsaturated phospholipid, L-α-dioleoylphosphatidylethanolamine, by Fujiwara et al. (2002) and Murase et al. (2004) for NRK and FRSK cells, respectively. The distributions of the side lengths for NRK (Fig. 8, pink closed bars) and FRSK (blue closed bars) cells are shown in the histograms in Fig. 8. The median values of the compartment area and the side length are 4.3×10^4 nm^2 and 230 nm, respectively, for NRK cells and 2.1×10^3 nm^2 and 41 nm, respectively, for FRSK cells (Murase et al., 2004).

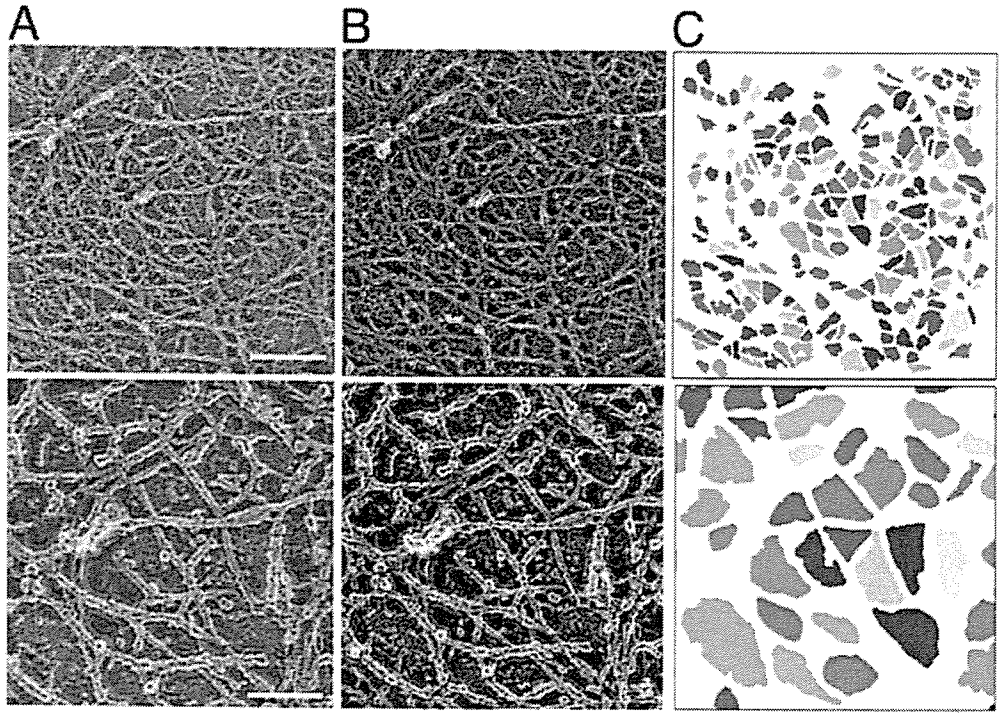

Figure 7. **The MSK meshwork directly on the cytoplasmic surface of the plasma membrane.** The central parts of the figures in the top row (bar, 300 nm) are magnified by a factor of three and are shown in the bottom row (bar, 100 nm). (A) Typical stereo views of the plasma membrane specimen (anaglyph; left = red). (B) Normal electron micrographs of the plasma membrane samples. The same view fields as those in A. (C) The areas delimited by the actin filaments closely apposed to the cytoplasmic surface of the cell membrane are shown. Different colors are shown to help the eye.

These results indicate that in the same cell line (for both the NRK and FRSK cases), the MSK mesh size determined by electron tomography and the diffusion compartment size determined by the high speed single-particle tracking of a phospholipid are similar to each other. However, between these two cell lines, both the MSK mesh and the diffusion compartment sizes differ greatly. The similarities between the MSK mesh sizes and the diffusion compartment sizes in cell lines that exhibit quite different distributions strongly support the MSK fence and picket models.

Discussion

We performed quantitative analyses of the undercoat structure of the cytoplasmic surface of the plasma membrane using electron tomography for samples prepared by a rapid-freeze, deep-etch, platinum replication technique. One of the most important limitations of this technique is that the cell has to be placed in a hypotonic medium at 4°C for 5–15 min to remove the upper cell membrane. However, with this method, large membrane fragments that were covered by the dense MSK meshwork could be obtained, which was important for the purpose of the present research.

We obtained the results by specifically addressing the following three questions. (1) Does the dense meshwork of the MSK exist everywhere on the cytoplasmic surface of the cell membrane, and, if so, how is it linked to the bulk cytoskeleton? (2) If so, what is its relationship with other structures of the plasma membrane, such as CCPs and caveolae? (3) How is the distribution of the MSK mesh size right on the cytoplasmic surface of the plasma membrane?

The final point is important because this part of the MSK might form the corrals of the plasma membrane for the diffusion of membrane molecules. Therefore, it is interesting to compare the distribution of the mesh size of the MSK directly attached to the cytoplasmic surface of the plasma membrane, as determined by an EM method, with that of the compartment size for the diffusion of membrane molecules. NRK (median size = 230 nm) and FRSK (41 nm) cell lines were selected for such a comparison because their compartment sizes are very different (Fujiwara et al., 2002; Murase et al., 2004). This will be an interesting test for the MSK fence and MSK-anchored transmembrane protein picket models and became possible by obtaining the 3D reconstructed images of the MSK structure on the cytoplasmic surface of the plasma membrane.

Does the dense meshwork of the MSK exist everywhere on the cytoplasmic surface of the cell membrane, and, if so, how is it linked to the bulk cytoskeleton?

The cytoplasmic surface of the plasma membrane has been observed by EM for >30 yr (Byers and Porter, 1977). Stunning high resolution EM images of the structures near the cytoplasmic surface have been published previously (Heuser and Kirschner,

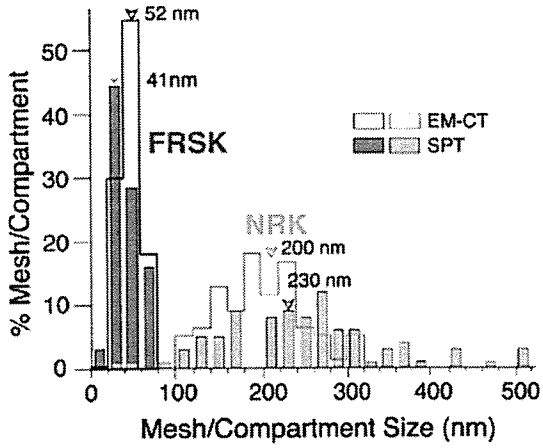

Figure 8. **Comparison of the distributions of the MSK mesh size on the cytoplasmic surface of the plasma membrane estimated by electron tomography with that of the compartment size determined from the phospholipid diffusion data for NRK and FRSK cells.** Electron tomography, open bars; phospholipid diffusion data, closed bars (adapted from Fujiwara et al., 2002 and Murase et al., 2004). NRK, pink; FRSK, blue. Within the same cell type, the MSK mesh size and diffusion compartment size exhibited similar distributions (compare the open and closed bars with the same color). The actual sizes are quite different between NRK and FRSK cells. EM-CT, EM-based computer tomograph; SPT, single-particle tracking.

1980; Hirokawa and Heuser, 1981; Heuser and Anderson, 1989; Hartwig and DeSisto, 1991; Rothberg et al., 1992), suggesting that the plasma membranes of animal cells are shaped by cytoskeletal interactions. However, despite these interesting and important studies, we felt that more extensive studies addressing the questions posed in the title of this subsection are necessary in particular for cells in culture.

We found that almost the entire cytoplasmic surface of the upper cell membrane is covered with the actin-based MSK except for the places where CCPs, caveolae, and noncoated membrane invaginations exist. In addition, this extensive pseudo-2D–type MSK network is linked to many actin filaments that extend from the membrane cytoplasmic surface toward the cytoplasm (Fig. 4 A) and is probably connected to the bulk cytoskeleton. This is consistent with the quantitative analysis of bleb formation, in which the density of the MSK filaments must be higher than one every 0.5–1 μm to avoid blebbing (Sheetz et al., 2006).

How closely is the MSK associated with CCPs and caveolae?

Almost all of the CCPs and caveolae are extensively linked to the MSK meshwork. As found in Figs. 2–4, many actin filaments that come out of the MSK meshwork are connected to these structures at their polygonal and striated patterns, respectively, and, in the cell types examined here, this occurs much more extensively than found previously (Rothberg et al., 1992; Fujimoto et al., 2000; Parton, 2003). Merrifield et al. (2002) found that actin rapidly becomes more concentrated at the CCPs right before they are internalized, but from the structures found in the present research, we could not tell what kind of actin–CCP interactions may be involved in such concentrations.

Is the distribution of the MSK mesh size right on the cytoplasmic surface of the plasma membrane consistent with that for the compartment size determined by a phospholipid diffusion probe?

3D reconstruction of the MSK using electron tomography allowed the determination of the MSK meshwork directly situated on the cytoplasmic surface of the plasma membrane. This meshwork is likely to partition the plasma membrane into many small compartments with regard to the lateral diffusion of membrane molecules. The size distribution of the areas bounded by the MSK meshwork agreed well with that determined for an unsaturated phospholipid undergoing hop diffusion in high speed single-particle tracking experiments in both NRK and FRSK cells, which have quite different mesh sizes (Fig. 8). These results support the MSK fence (corralling) model and the anchored transmembrane protein picket model.

How the MSK is attached to the cytoplasmic surface of the plasma membrane is unknown. Specific proteins that link the membrane and actin filaments at their barbed ends, such as gelsolin and villin (Pollard and Cooper, 1986; Hartwig et al., 1989), and at their sides, such as ponticulin (Wuestehube and Luna, 1987) and ezrin/radixin/moesin family proteins (Tsukita et al., 1997), exist. However, the weak nonspecific binding of actin filaments to membrane lipids and proteins may greatly contribute to the interactions of the actin filaments with the membrane. Although transmembrane proteins are temporarily trapped within a compartment, they hop to adjacent compartments in longer terms, suggesting that the link between the membrane and actin filaments may break at a rate comparable with the hop rate, which is once every several to several hundred milliseconds (depending on the molecule and cell type).

In addition to actin and actin-associated proteins, some other proteins may contribute to forming the MSK and membrane corrals. For example, septin, which is ~7-nm thick in the negatively stained images (Kinoshita et al., 2002), and agorin (Apgar and Mescher, 1986) may play some roles. Further characterization of the proteins involved in the MSK and its interaction with the membrane components and further analysis of the dynamics of membrane–MSK interactions will be important for understanding the roles played by the MSK–plasma membrane interactions in signal transduction, domain formation in the plasma membrane, and reorganization of the cytoskeleton.

Materials and methods

Antibodies and other reagents

Rabbit anti-actin IgG was obtained from Biomedical Technologies, and colloidal gold probes (5-nm diameter) coated with secondary antibodies (produced in goat) were purchased from GE Healthcare.

Rapid-freeze, deep-etch, immunoreplica EM of the cytoplasmic cell surface

NRK and FRSK cells were maintained in HAM-F12 or DME mediums, respectively, supplemented with 10% FBS (Sigma-Aldrich) under a 5% CO_2 atmosphere at 37°C. The cells used for the experiments were grown in 35-mm plastic dishes to ~70% confluency, usually 2 d after inoculation. The cells were washed three times with ice-cold Pipes buffer (10 mM Pipes, 100 mM KCl, 5 mM $MgCl_2$, and 3 mM EGTA, pH 6.8, which mimics the environment in the cytoplasm somewhat but is slightly hypotonic) and were exposed for 15–30 s to an ice-cold 70% Pipes buffer (the Pipes buffer diluted by a factor of 1.43 with water, making this solution more hypotonic;